Contribution of ground ice melting to the expansion of ~~Serling~~Selin Co (lake) on the Tibetan Plateau

Lingxiao Wang[1], Lin Zhao[1,2], Huayun Zhou[2,3], Shibo Liu[2,3], Erji Du[2], Defu Zou[2], Guangyue Liu[2], Yao Xiao[2], Guojie Hu[2], Chong Wang[1], Zhe Sun[2], Zhibin Li[1], Yongping Qiao[2], Tonghua Wu[2], Chengye Li[1], Xubing Li[1]

[1]School of Geographical Sciences, Nanjing University of Information Science & Technology (NUIST), Nanjing 210044, China
[2]Cryosphere Research Station on Qinghai-Xizang Plateau, State Key Laboratory of Cryosphere Science, Northwest Institute of Eco-Environment and Resources, Chinese Academy of Sciences (CAS), Lanzhou, 730000, China
[3]University of Chinese Academy of Sciences, Beijing, China

Correspondence to: Lin Zhao (lzhao@nuist.edu.cn)~~ and Lingxiao Wang (lx.wang@nuist.edu.cn)~~

Abstract. ~~Serling~~Selin Co~~ lake, surrounded by ~~, located within permafrost ~~and glacier-occupied ~~regions surrounded by glaciers, has exhibited the greatest increase in water storage ~~over the last 50 years ~~among all the lakes on the Tibetan Plateau~~. However, increases in precipitation and glacial melting are not enough to explain ~~ over the last 50 years. Most of the increased lake water volume ~~of lake expansion. The magnitude of ~~has been attributed to increased precipitation and the ~~contribution~~accelerated melting of glacier ice, but these processes are still not sufficient to achieve the water balance with the expansion of Selin Co. Ground ice meltwater released by thawing permafrost due to ~~this increase under~~continuous climate warming ~~remains unknown. ~~over the past several decades was regarded as another source of lake expansion. This study ~~made~~presented the first attempt to quantify the water contribution of ground ice melting to the expansion of ~~Serling~~Selin Co~~ lake~~ by evaluating the ground surface deformation. We monitored the spatial distribution of surface deformation in the ~~Serling~~Selin Co basin using the SBAS-InSAR technique and compared ~~it~~the results with the findings of field surveys. Then, the ground ice meltwater volume in the watershed was calculated based on the ~~long-term deformation rate.~~cumulated settlement. Finally, this volume was compared with the lake volume change during the same period, and the contribution ratio was derived. SBAS-InSAR monitoring during 2017–2020 illustrated widespread and large subsidence in the upstream section of the Zhajiazangbu subbasin, where widespread continuous permafrost is present. The terrain subsidence rate was normally between 5 and 20 mm/a, indicating rapid ground ice loss in the region. The ground ice ~~meltwater~~melted water reached ~~56.0~~a rate of 57.4×10^6 m^3/a, and the rate of increase in lake water storage was ~~496.3~~485×10^6 m^3/a during the same period, with ground ice meltwater contributing 11.~~3~~8% of the lake volume increase. This study is especially helpful ~~in~~for explaining the rapid expansion of ~~Serling~~Selin Co~~ lake~~ and equilibrating the water balance at the watershed scale. More importantly, the proposed method can be easily extended to other watersheds underlain by permafrost and to help understand the ~~hydrologic~~hydrological changes in these watersheds.

Keywords: surface deformation, SBAS-InSAR, permafrost, ground ice, ~~Serling~~Selin Co~~ lake~~, expansion

1. Introduction

~~More than 1000 lakes on the Tibetan Plateau span an area exceeding 1 km^2, and the total lake area is greater than 40,000 km^2 (Wan et al., 2016).~~More than 1200 lakes on the Tibetan Plateau (TP) span an area exceeding 1 km^2, and the total lake area is greater than 46000 km^2 (Zhang et al., 2021b). The water in most of these lakes is more or less connected with widely distributed glaciers and permafrost. Recent studies have indicated that most of the lakes on the ~~Tibetan Plateau~~TP have manifested extensive changes (Qiao et al., 2019; Zhang et al., 2020). ~~In particular, Serling Co (Siling Co) lake exhibited the greatest increases in the lake area and water storage: its lake area expanded by 43% from 1,667 km^2 in 1976 to 2389 km^2 in 2017, and its water storage increased by 80% from 309.4 ×10^8 m^3 in 1972 to 558.4 ×10^8 m^3 in 2017 (Yang et al., 2017; Zhu et al., 2019). Its lake area surpassed Nam Co lake in 2014 and is now the second largest saltwater lake in China. Such rapid changes in Serling Co lake have exerted significant effects on the regional environment and have~~In particular, Selin Co (also known as Siling Co, Serlin Co, and Serling Co) exhibited the greatest increases in both lake area and water storage: its lake area expanded by ~40% from ~1700 km^2 in 1972 to ~2400 km^2 in 2020, and its water storage increased by 80% from 309.4×10^8 m^3 in 1972 to 558.4×10^8 m^3 in 2017 (Zhu et al., 2019b; Zhang et al., 2021b). Its lake area surpassed that of Nam Co in the early 2000s (Zhang et al., 2021b; Bian et al., 2010); consequently, Selin Co is now the second largest saltwater lake in China. Such rapid changes in Selin Co have significantly affected the regional environment and have thus attracted substantial interest within the scientific community.

~~The entire Serling Co watershed covers a drainage area of 4.4×10^4 km^2 and hosts 642 glaciers with a total area of 593.1 km^2 and ice reserves of 36.4 km^3 (Bian et al., 2010; Shi et al., 2005). The watershed has a large permafrost distribution, including both continuous permafrost and seasonally frozen ground covering an area of 1.3×10^4 km^2, with the former being widespread mainly in the northern part of the watershed (Zou et al., 2017). Based on a map of the ground ice distribution across the Qinghai-Tibet Plateau, the ground ice volume in the watershed reaches 132.3 km^3 (Zhao and Sheng, 2019). To reveal the potential reasons for the abovementioned rapid expansion of lakes on the plateau, an accurate estimation of the basin water balance is urgent (Lei et al., 2014; Zhang et al., 2017; Li et al., 2014; Song et al., 2014). Glacial meltwater, the thawing of permafrost, precipitation (including snow) and changes in evapotranspiration all contribute to lake recharge. A model simulation of endorheic basins on the Tibetan Plateau showed that increased net precipitation contributed the majority of the water supply (~70%) for the increased lake volume (Zhang et al., 2017). In addition, recent research has revealed that glacial meltwater contributed ~ 10% of the total water input to Serling Co lake since the 1970s (Lei et al., 2013; Tong et al., 2016). The weakening of lake evaporation has also contributed to the accelerated expansion of Serling Co lake to some extent, but this contribution is small (Guo et al., 2019). In contrast, the contribution of thawing permafrost to lake expansion remains poorly quantified.~~

The entire Selin Co watershed covers a drainage area of 4.4×10^4 km^2, 18 times the lake surface. Accordingly, a lake water level increase of 0.2 m/a corresponds to at least 1 cm/a of water collected uniformly over the whole watershed area (neglecting evaporation). The entire watershed hosts 299 glaciers with a total area of 369.7 km^2 and ice reserves of 27.9 km^3 based on the second Chinese glacier inventory (Guo et al., 2015; Liu et al., 2012b); additionally, according to the new estimation by (Farinotti et al., 2019), the glacier volume reaches 21.8 km^3 in the watershed. (Zou et al., 2017) mapped the permafrost distribution on the Qinghai-Tibet Plateau (QTP) based on freezing and thawing indices from Moderate Resolution Imaging Spectroradiometer (MODIS) land surface temperatures and validated their map using various ground-based datasets; according to this permafrost map, the permafrost area covers ~1.3×10^4 km^2, accounting for 30.2% of the watershed. Continuous permafrost and seasonally frozen ground exist, with the former being widespread mainly in the northern part of the watershed (Zou et al., 2017). (Zhao and Sheng, 2019) estimated the ground ice storage on the QTP based on the ice content distribution characteristics from 164 drill core records deeper than 15 m, the above permafrost distribution map, a map of the Quaternary sedimentary types, and a permafrost thickness map; based on their map, the ground ice volume in the watershed reaches 132.3 km^3 (Zhao and Sheng, 2019), approximately five times the glacier ice volume in the Selin Co watershed.

To reveal the potential reasons for the abovementioned rapid expansion of lakes on the TP, an accurate estimation of the basin water balance is urgently needed (Lei et al., 2014; Zhang et al., 2017; Li et al., 2014; Song et al., 2014). Glacial meltwater, the thawing of permafrost, precipitation (including snow) and changes in evapotranspiration all contribute to lake recharge. A model simulation of endorheic basins on the TP showed that increased net precipitation contributed the majority of the water supply (~70%) to the increased lake volume (Zhang et al., 2017). In addition, recent research has revealed that glacial meltwater has contributed ~ 10% of the total water input to Selin Co since the 1970s (Lei et al., 2013; Tong et al., 2016; Brun et al., 2020; Zhang et al., 2021a). The weakening of lake evaporation during 1972–2010 due to decreasing wind speeds also contributed to the accelerated expansion of Selin Co to some extent, but this contribution was reported to be very small (Guo et al., 2019).

Significant permafrost degradation has been observed on the Tibetan PlateauTP under athe impacts of the warming climate. The monitoring of ten boreholes on the Tibetan PlateauTP revealed that from 1981 to 2018, the active layer thickened at an average rate of 19.5 cm per decade; moreover, this thickening trend has been accelerating in recent years (Zhao et al., 2020). The thawing of the ice-rich permafrost layer just below the permafrost table releases a certain amount of water into the hydrological cycle (Zhao et al., 2019). Some studies have suggested that. In the meantime, different permafrost regions across the TP experienced thaw settlements (Daout et al., 2017; Chen et al., 2022). The ice content within the uppermost layer of permafrost is typically higher than the saturated water content after this permafrost layer thaws; hence, the thawing of this layer might result in terrain settlement (Streletskiy et al., 2016; Shiklomanov et al., 2013; Günther et al., 2015; Lantuit and Pollard, 2008; Kokelj and Jorgenson, 2013). The terrain settlement was attributed to the melting of ground ice from the ice-rich permafrost layer just below the permafrost table and the further release of this water into the hydrological cycle (Zhao et al., 2019).

The melting of ground ice released water into the hydrological cycle (Zhao et al., 2019; Jin et al., 2022), hence permafrost degradation might be a possible source of the water that is causing lakes to expand (Li et al., 2014), but this contribution has yet to be quantified. ~~Under the dramatic hydrometeorological changes observed in recent decades, quantifying the contribution of thawing permafrost is not an easy task.~~By separating hydrographs using isotopes, some researchers calculated the contributions of meltwater from ground ice to surface water runoff~~ by separating hydrographs using isotopes~~ and found that the contribution ranged from 13.2% to 16.7% in the source region of the Yellow River (Yang et al., 2019), and that to nearby thermokarst lakes in the Beiluhe region reached 61.3% (Yang et al., 2016). ~~Some studies estimated the~~The amount of meltwater from permafrost degradation was also modeled by ~~modeling~~multiplying the active layer thickening rate and~~ then multiplying the result by~~ the average ground ice content (Zhang et al., 2017).

Interferometric synthetic aperture radar (InSAR) analysis can exploit the phase changes in SAR signals to determine relative surface displacements on the order of millimeters to centimeters. Accordingly, InSAR monitoring can detect the terrain subsidence triggered by the thawing of ice-rich permafrost, e.g., ~~The ice content within the uppermost layer of permafrost is typically higher than the saturated water content after this permafrost layer thaws; hence, the thawing of this layer might result in the terrain settlement (Streletskiy et al., 2016; Shiklomanov et al., 2013), slumping, or collapse of the ground surface~~ (Daout et al., 2020; Zwieback and Meyer, 2021; Chen et al., 2018; Lu et al., 2020; Liu et al., 2012a). Permafrost regions with higher ground ice contents have been shown to produce greater terrain subsidence on the TP (~~Günther~~Wu et al., ~~2015; Lantuit and Pollard, 2008; Kokelj and Jorgenson, 2013~~2018; Daout et al., 2017; Chen et al., 2018)~~.~~ ~~Interferometric synthetic aperture radar (InSAR) analysis can exploit the phase changes in SAR signals to determine the relative surface displacement on the order of millimeters to centimeters.~~ . The subsidence rate is less than 5 mm/a in the northwestern TP, where the climate is cold and dry (Daout et al., 2017), while it is up to 30 mm/a on the ice-rich Eboling Mountain in the northeastern region of the TP (Chen et al., 2018).

~~Accordingly, InSAR monitoring can detect the terrain subsidence triggered by the thawing of ice-rich permafrost, e.g., (Daout et al., 2020), (Zwieback and Meyer, 2021), (Chen et al., 2018),(Lu et al., 2020), (Liu et al., 2012). Permafrost regions with higher ground ice contents have been shown to produce greater terrain subsidence on the Tibetan Plateau (Wu et al., 2018; Daout et al., 2017; Chen et al., 2018). The long-term subsidence rate is less than 5 mm/a on the northwestern Tibetan Plateau, where the climate is cold and dry (Daout et al., 2017), while it ranges from 3 to 30 mm/a on the ice-rich Eboling Mountain in the northeastern region of the Tibetan Plateau (Chen et al., 2018). Such long-term terrain subsidence in permafrost regions is~~

~~mostly the consequence of the thawing of the ice-rich permafrost layer under warming climate conditions (Zhao et al., 2019).~~

In this study, we ~~present~~conducted the first attempt to quantify the contribution of ground ice melting ~~ground ice~~ to the expansion of the ~~Serling~~Selin Co watershed~~. We hypothesize~~ through surface settlement. It is well known that the ~~long-term ground subsidence in this watershed is related to the subsurface depth of ground ice melting~~permafrost layer just below the permafrost table always contains ground ice higher than 50% in volume (Cheng, 1983; Mackay, 1983; French and Harbor, 2013; Zhao and Sheng, 2019). Therefore, we assumed that the amount of surface settlement would release the same amount of ground ice caused by compressing the thawing ice-rich permafrost layer. The spatial distribution of surface deformation was derived through InSAR analysis and compared with the findings of field surveys. Finally, the ground ice meltwater volume in the watershed was compared with the ~~Serling~~Selin Co~~ lake~~ volume increase, and the contribution ratio was determined.

2. Study area and data resources

2.1 Study area

The ~~Serling~~Selin Co watershed, which is in the transitional zone between the Indian monsoon and the westerlies over the ~~Tibetan Plateau~~TP, is ~~situated in~~characterized by a cold semiarid monsoon climate with a mean annual temperature of approximately 0°C~~, an~~ and average precipitation of ~350 mm (Tong et al., 2016). From 1979 to 2017, the average annual temperature increased at a rate of 0.049°C/a, and the average annual precipitation increased at a rate of 4.65 mm/a, with the main increase occurring after the mid-1990s ~~(Zhu et al., 2019)~~(Zhu et al., 2019b).

This watershed basin extends over a total area of approximately 4.4×10^4 km^2, and the rivers and lakes within the basin are connected, forming an inland lake group. Ngoin Co is located south of ~~Serling~~Selin Co, while Wuru Co & Qiagui Co are located west of ~~Serling~~Selin Co; their locations are marked as ② and ③, respectively, in Fig. 1. The main rivers ~~entering~~draining into the lake are the Zhajiazangbu (from the north ~~into~~), the ~~lake),~~ Zhagenzangbu ~~(west),~~and Alizangbu (from the west), and the Boquzangbu (from the east) (Tong et al., 2016), as shown in Fig. 1. The details of the four major subbasins and the inflows of the runoff from these rivers into the lake are listed in Table 1. The Zhajiazangbu river with a length of 409 km originates from the Tanggula Mountains and enters ~~Serling~~Selin Co ~~lake~~ from the north. Widespread continuous permafrost occurs mainly in the northern part of the basin, whereas sporadic permafrost and seasonally frozen ground are found in the central and southern parts of the watershed. Among the four subbasins, the Zhajiazangbu has the largest permafrost distribution (10667 km^2~~,~~ or 66.2% of the subbasin area), followed by the Zhagenzangbu (1967 km^2~~,~~ or 12.3% of the subbasin area) (Zou et al., 2017).

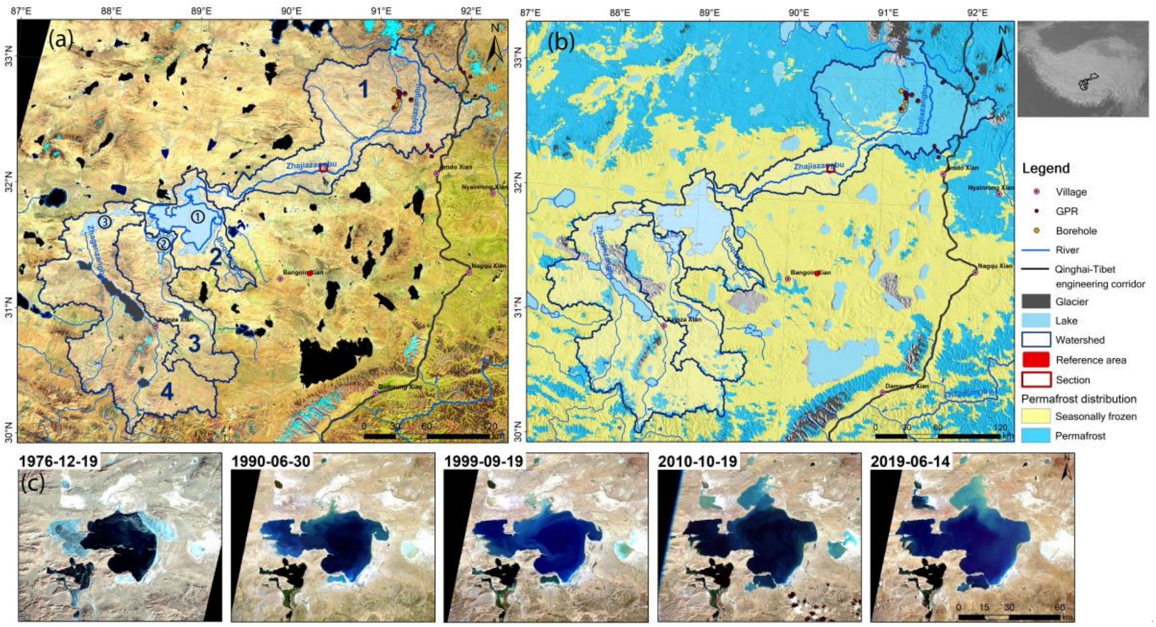

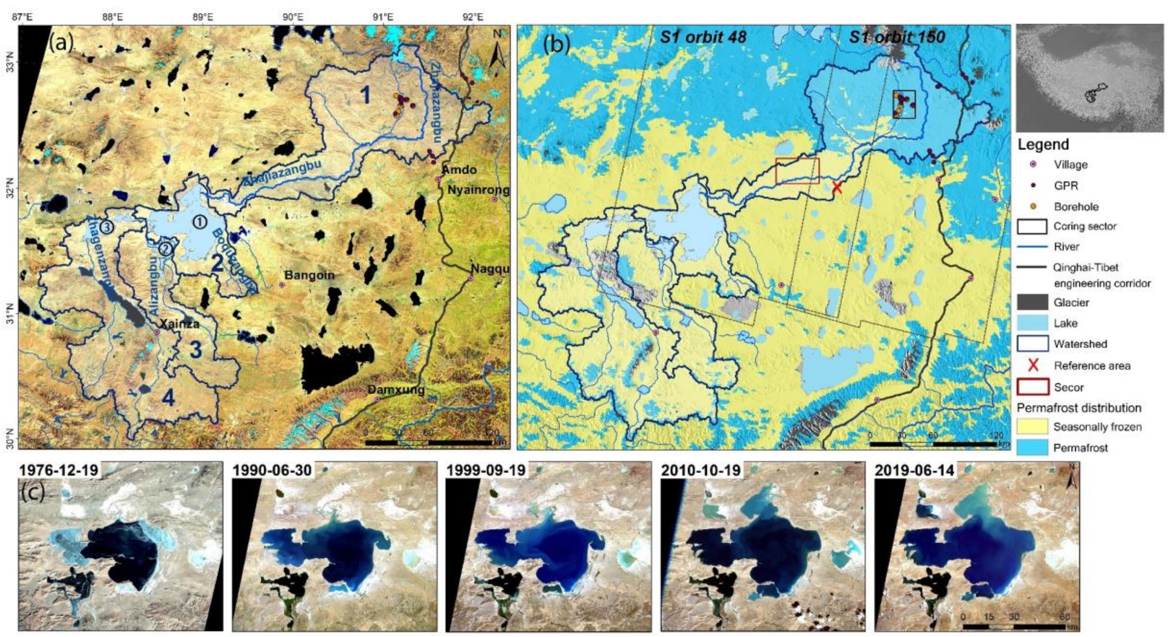

Figure 1 Study area. The base map in Fig. 1(a) is a Landsat 8 image acquired in October 2020 (red: SWIR1, green: NIR, blue: red). The base map in Fig. 1(b) is a permafrost map (Zou et al., 2017); the hillshade is calculated using a 1-arcsec SRTM DEM with the Sentinel-1 incidence angle and azimuth angle. ~~The red dot~~The grey dashed lines delineate two tracks of Sentinel-1 used in this study. The red cross marks the position of our InSAR reference point. The locations of the GPR surveys and boreholes are shown with dots. Fig. 1(c) shows the lake areas from 1976 to 2019 on Landsat optical images.

Table 1 Characteristics of the ~~Serling~~Selin Co ~~lake~~ basin.

Basin	Area (km^2)	~~Ave.~~Average elevation	Permafrost coverage

			(m~~)~~ a.s.l.)	Area (km^2)	Percentage of subbasin area (%)	Percentage of the entire basin area (%)
1	Zhajiazangbu subbasin	16112	4963	10667	66.2	24
2	Boquzangbu subbasin	5474	4651	124	2.3	0.3
3	Alizangbu subbasin	6831	4951	646	9.5	1.5
4	Zhagenzangbu subbasin	16019	5022	1967	12.3	4.4
	Entire basin	44437	4944	13404		30.2

2.2 Field data

We conducted a field investigation of the permafrost in the study area ~~during the autumn months of~~in October 2019. ~~During the fieldwork, we drilled~~ Seven boreholes deeper than 20 m were drilled, and ~~carried out~~ ground-penetrating radar (GPR) surveys~~. Boreholes with depths deeper than 20 m were drilled~~ were carried out in the upstream section of the Zhajiazangbu subbasin~~; their~~ (locations are marked in Fig. ~~1,~~1). The survey was performed at the end of the thawing period, allowing us to estimate the maximum thawing depth and ~~their descriptions~~the location of the permafrost table. The permafrost table was estimated from the cores of the boreholes, and the development of ground ice was described as well. Descriptions of the boreholes are provided in Table 2~~.~~, and field photographs of the cores at borehole sites SLC01 and SLC04 are shown in Fig. 2.

Twenty 50-m-long GPR ~~profile surveys~~profiles were carried out within or around the catchment, fourteen of which were within the basin. Based on the fourteen GPR ~~reflection~~ profiles carried out within the basin, the permafrost ~~active layer has~~table was at a maximum ~~thickness~~depth of 4.1 m, a minimum depth of 2.0 m, and an average ~~value~~depth of 3.2 m. The volumetric soil water content in the active layer ~~ranges~~ranged from a maximum of 46.4% to a minimum of 14.7%, with an average of 22.6% based on ~~GPR~~our interpretation of the GPR data.

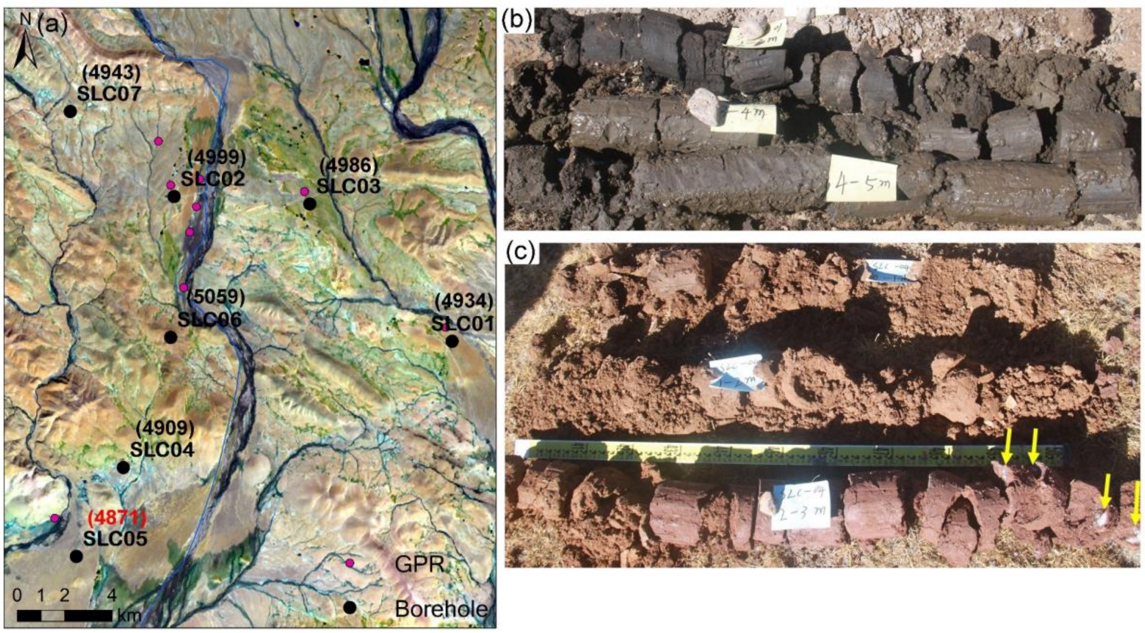

Figure 2 <u>(a) Locations of surveyed sites. The base map is Landsat 8 image acquired in October 2020. For borehole sites, their elevations (m a.s.l.) are labeled in brackets. Site SLC05 has no permafrost.</u> **Cores from borehole SLC01 at depths of 2–~~5~~5 m (a) and SLC04 at depths of 0–3 m (b). Ice blocks were found in SLC04 at a depth of 2.4 m, as indicated by the arrows in (b).**

Table 2 Borehole properties.

Site	Permafrost table <u>depth</u> (m)	Topography	Surface	Development of ground ice
SLC01	3.0	floodplain	alpine meadow veg coverage: 40%,	Not found

			surface soil is sandy, dry	
SLC02	3.6	river terrace	degraded alpine steppe, sparse vegetation, surface soil is sandy, dry	ice at depths of 3.6–5.5 m
SLC03	3.0	river valley	alpine swamp meadow, veg coverage: 90% high water content in the active layer	ice at 2.4–3.0 m, large amounts of liquid water found at 3.0–4.5 m, ice lenses at 4.6–5.1 m
SLC04	< 2.4	river valley terrace, approximately 500 m away from the river	alpine swamp meadows veg coverage: 90%	ice at 2.4 m, pure ice layer (~3 cm) at 4.2–4.3 m, ~~and~~ ice lenses at 6–7.7 m
SLC05	~~NA~~N/A seasonally frozen ground	river valley in between two rivers	alpine steppe veg coverage: 30%, surface soil is sandy and contains abundant gravel	not found
SLC06	unclear	top of slope	alpine meadow veg coverage: 50%, surface soil is sandy and contains abundant gravel	ice at 6–7.8 m
SLC07	unclear	middle of a very gentle slope	degraded alpine meadow, very sparse veg surface soil is sandy and contains abundant gravel, severely salinized	liquid water found at 2.5–6.5 m ~~and~~, a large amount found at 2.5–3.5 m

2.3 Sentinel-1 SAR images

Sentinel-1 (S1) C-band SAR images (https://scihub.copernicus.eu/) were used to monitor the surface deformation. ~~Sentinel-1 is a C-band SAR mission that was~~ S1, a constellation comprising two satellites launched in 2014 (S1A) and 2016 (S1B~~). It is a constellation of two satellites orbiting~~) that orbit the Earth ~~and has been~~ , is a C-band SAR mission that was developed and is operated by the European Space Agency (ESA) ~~within~~as part of the Copernicus program. VV-polarized Level 1 single look complex (SLC) images ~~of~~acquired in interferometric wide-swath (IW) mode ~~with VV polarization in the~~in descending orbit were used in the study. The study area ~~covers~~is covered by two orbits of S1 acquisitions, ~~and~~ the details of which are shown in Table 3. In total, 95 acquisition dates for descending orbit 48 and 100 acquisition dates for descending orbit 150 from September 2017 to December 2020 were processed.

Table 3 Information on ~~Sentinel-1~~the S1 images processed to monitor the surface deformation.

	Orbit 48	**Orbit 150**

Frame	489, 484, 479	490, 485, 480
Incidence angle ~~(degree~~range (degrees)	31.85–46.32	31.57–46.27
Acquisition period	~~2017-09-11~~20170911 to ~~2020-12-24~~20201224	~~2017-09-05~~20170905 to ~~2020-12-30~~20201230
Number of acquisition dates	95	100

2.4 SRTM DEM

A 1-arcsecond grid (~30-m) Shuttle Radar Topographic Mission (SRTM) digital elevation model (DEM) was used to calculate the slope, and ~~to~~ remove the topographic phase and implement geocoding during InSAR processing.

2.5 ICESat-2 dataset

Laser altimetry data ~~of~~from the ICESat-2 ATL13 product (https://nsidc.org/data/atl13) were applied to extract the water surface ~~elevation~~elevations of the lakes.

2.6 Landsat 8 Operational Land Imager (OLI) images

Optical Landsat 8 OLI ~~optical~~ images (https://glovis.usgs.gov/) were used to detect ~~lake extent~~ changes~~.~~ in the lake extents. Cloud-free images acquired during autumn or summer ~~with no influence of the cloud~~ were selected~~.~~, and the acquisition ~~dates~~date and path/row of ~~these images~~each image are listed in Table 4.

Table 4 Information on the Landsat 8 images used.

Lake	2015	2016	2017	2018	2019	2020
~~Serling~~Selin Co	p140r037~~_20151117~~ D20151117	p139r038~~_20161112~~ D20161112	p139r038~~_20170928~~ D20170928	p139r038~~_20181001~~ D20181001	p139r038~~_20190614~~ D20190614	p139r038~~_20201006~~ D20201006
Ngoin Co	p140r038~~_20150930~~ D20150930	p139r038~~_20161112~~ D20161112	p139r038~~_20170928~~ D20170928	p140r038~~_20181109~~ D20181109	p140r038~~_20190925~~ D20190925	p140r038~~_20201013~~ D20201013
Wuru Co & Qiagui Co	p140r038~~_20150930~~ D20150930	p140r038~~_20161103~~ D20161103	p140r038~~_20171005~~ D20171005	p140r038~~_20181109~~ D20181109	p140r038~~_20190925~~ D20190925	p140r038~~_20201013~~ D20201013

"p" denotes the path~~ and~~, "r" denotes the row of the frame, and "D" denotes the acquisition date.

3 Methodology

3.1 Workflow

An overview of the methodology employed in this study is illustrated in Fig. 3. The main steps are summarized as i) retrieval of lake water storage changes, ii) retrieval of deformation time series, iii) estimation of the ground ice meltwater volume from the long-term deformation rate, and iv) calculation of the ratio of the water volume contributed by permafrost ground ice melting to the increase in lake water storage. The ~~detailed~~ processing steps are described in detail in the following subsections.

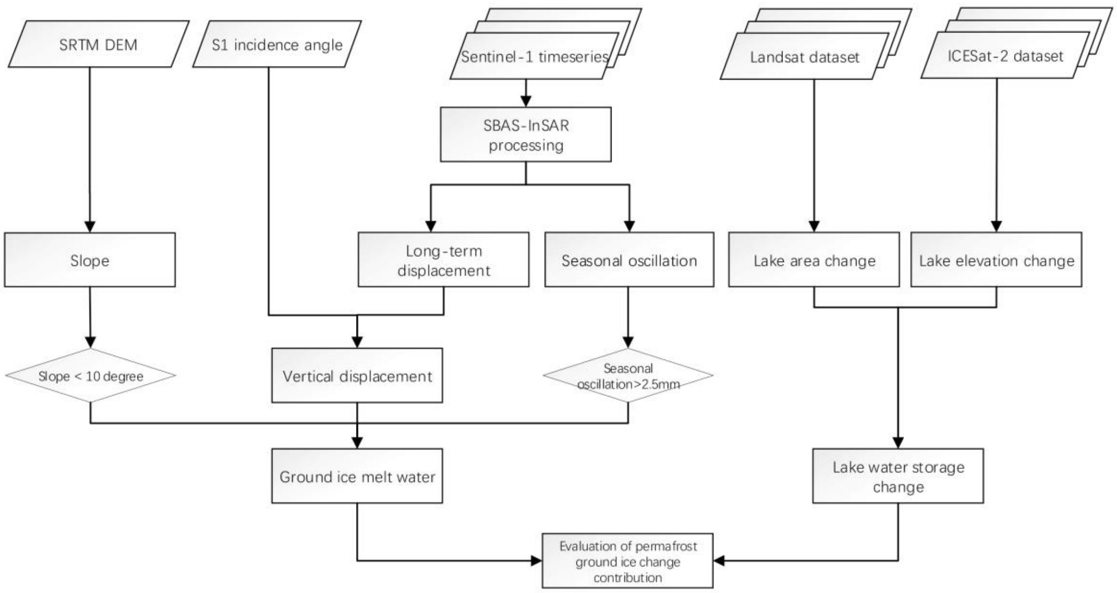

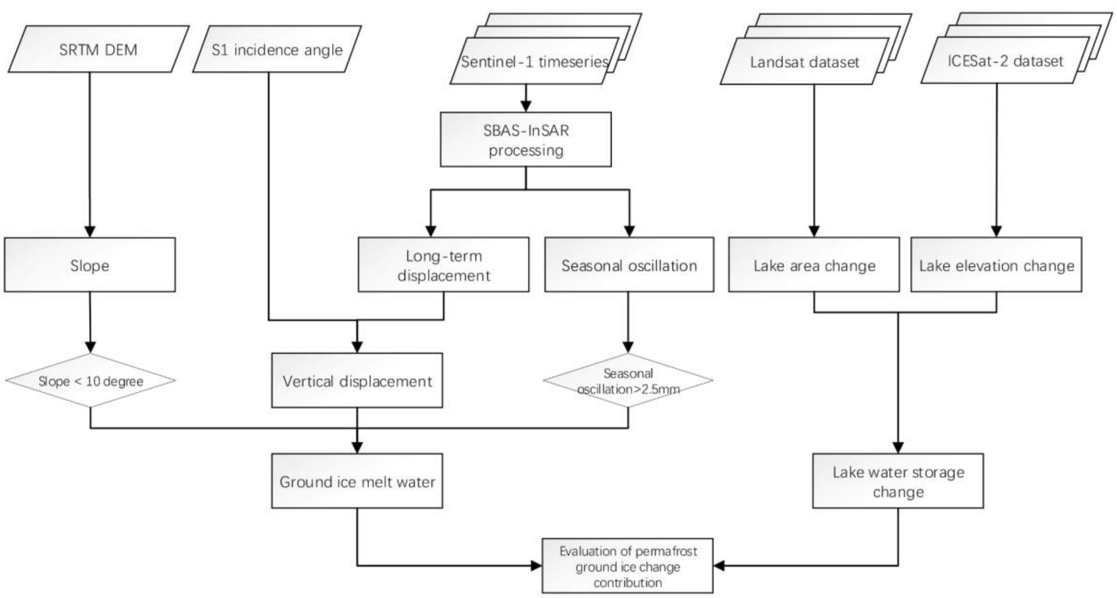

Figure 3 Workflow of estimating the water contribution ~~of~~by permafrost ground ice melting to the expansion of ~~Serling~~Selin Co ~~lake~~.

3.2 Lake water storage ~~change~~changes

First, we retrieved ~~the~~water surface ~~water level elevation~~elevations through the ICESat-2 ATL13 laser altimetry ~~ICESat-2 ATL13~~ product~~.~~ by extracting data values within ~~the lake~~each lake's area ~~were extracted~~ from 13 October 2018 to the end of 2020. For each year, the mean annual ~~value~~elevation was calculated from all data acquisitions during the year. The lake water level change rate was then estimated by a linear trend model.

Then, we extracted the lake area extent using Landsat 8 OLI images in 2018, 2019, and 2020. Three bands (NIR, SWIR1, and SWIR2) were stacked to extract the lake area because lake water has extremely low reflectance ~~at~~in these bands and thus is easily separated from other land cover types. K-means clustering was then applied to classify the land cover types in the stacked image into two classes: water and other~~ land covers~~. After that, a 3×3 window size majority filtering was applied as a postprocessing step, and we then converted the classified image ~~to the~~into a shapefile and eliminated the spots outside the inlet and outlets of the ~~lake~~lakes. The lake areas in 2015, 2016 and 2017 were obtained from a previous study (Zhang, 2019); we also modified the lakes to have the same inlets and outlets. For lakes with irregular areas, their storage ~~can be~~was approximately calculated according to the volume of ~~the~~a circular platform~~, and then~~; thus, the change in the volume ~~change~~ of the lake ~~can be~~was calculated from the difference between the volumes of two circular platforms (Zhang et al., 2019a), as described in Eq. (1):

$$\Delta V = \frac{1}{3}(H_2 - H_1) \times \left(S_1 + S_2 + \sqrt{S_1 \times S_2}\right) \quad (1)$$

where ΔV is the change in lake water storage, S_1 and S_2 represent the lake areas ~~of~~during two periods (e.g., the lake areas in 2018 and 2020), and $(H_2 - H_1)$ represents the ~~lake level~~water surface elevation change between the two periods.

3.3 Deformation monitoring

3.3.1 SBAS-InSAR processing

~~Time series InSAR analysis was~~In this study, we implemented ~~using~~the small baseline subset (SBAS) time series InSAR analysis (SBAS-InSAR) technique, which deploys multiple master datasets to minimize the effects of ~~spatial-temporal~~spatiotemporal decorrelation (Berardino et al., 2002; Lanari et al., 2004; Usai, 2003) by selecting interferograms ~~having~~with small spatial and temporal baselines. Thus, this technique is suitable for permafrost environments prone to strong ~~spatial-temporal~~spatiotemporal decorrelation.

The ~~Serling~~Selin Co basin is covered by two orbits of S1 images. We processed the SBAS-InSAR analysis individually for each orbit. SBAS-InSAR processing in this study contains three main steps: i) InSAR processing of the images, including interferogram network selection, coregistration, differential interferogram phase generation and phase unwrapping; ii) deformation time series estimation; and iii) reference point refinement and geocoding.

The main processing steps are described in detail as follows:

i) InSAR processing

~~Every SAR image was coregistered with the next two sequential acquisitions.~~To overcome the decorrelation caused by changes in the permafrost landscape (e.g., freeze–thaw transitions and vegetation phenology), we generated interferograms with only short time intervals. The precision state vectors obtained from the ESA were applied to reduce the effects of inaccurate baselines. ~~To overcome~~All the ~~decorrelation caused by permafrost landscapes (mainly vegetation dynamics)~~SLC images were coregistered to the stack reference of 20180807 acquisition for orbit 150 and ~~terrain elevation changes, we generated only~~20180801 acquisition for orbit 48. After generating a coregistered stack of SLC images, interferograms were generated by each SAR image with ~~short time intervals.~~its two sequential acquisitions. The temporal baselines of the individual interferograms ~~are~~ranged from 12 to ~~24~~36 days, and the perpendicular baseline of all the interferometric pairs ~~is <100~~was < 200 m. ~~We then performed~~ Multilooking with 3 pixels in ~~range~~azimuth and 13 pixels in ~~azimuth~~ range was then performed to form a square pixel (~40 m) and reduce ~~the~~ noise. To remove the topographic phase, the topographic phase was simulated using the SRTM DEM and subtracted from the interferogram. ~~After that~~Next, we applied an adaptive spectral filter to produce differential interferograms. To unwrap the differential phase, ~~a minimum cost flow (MCF) phase unwrap method was applied. Two orbits covering an area of approximately 450 km × 500 km were processed. This processing was implemented using ISCE (https://github.com/isce-framework/isce2).~~the SNAPHU Minimum Cost Flow (MCF) phase unwrapping algorithm (Chen and Zebker, 2002) was applied. Two orbits covering an area of approximately 450 km×500 km were processed using ISCE software (https://github.com/isce-framework/isce2). To facilitate the processing of data over such a large area, coregistration and conversion between radar coordinates and geometric coordinate systems were accelerated by the aid of a ~~graphic~~graphics processing unit (GPU) under the Compute Unified Device Architecture (CUDA) framework~~ during the processing of such a large area.~~.

ii) Deformation time series estimation

In this step, the network of unwrapped interferograms was inverted to construct a timeline of line-of-sight (LOS) displacement maps. ~~We applied a weighted least square (WLS) estimator to invert the network of interferograms into time series. During the inversion, interferograms are weighted by the inverse of the phase variance (Guarnieri and Tebaldini, 2008; Tough et al., 1995). Different from some studies conducted in permafrost environments that presuppose deformation models to facilitate solving the phase time series, we did not preset any deformation and~~A multilook 2 by 2 was applied to interferograms to reduce dataset size. Before the network inversion, we applied unwrapping error corrections by bridging reliable regions (Zhang et al., 2019b). The interferograms, generated by each SAR image with its two sequential acquisitions, all have averaged interferometric coherence above 0.7. Appendix Fig. A1 presents an overview of the interferogam network and the averaged interferometric coherence. We applied a weighted least square (WLS) estimator to invert the network of interferograms into a time series. During the inversion, interferograms were weighted by the inverse of the phase variance of the whole interferogram (Zhang et al., 2019b). Different from some studies conducted in permafrost environments that presupposed deformation models to help solve the phase time series (Li et al., 2015; Chen et al., 2018), we did not preset any deformation and instead obtained the raw phase time series by minimizing the phase residual. The time series of LOS displacements are relative to the first scene of the datasets and spatially relative to the reference point. The reference point was ~~firstly~~first set by selecting pixels with extremely high temporal coherence greater than 0.99.

After the raw phase time series were obtained,~~ the~~ tropospheric delay correction, phase deramping, and topographic residual correction were applied. The tropospheric delay was estimated in the satellite LOS direction using ~~ERA-5 reanalysis data.~~European Centre for Medium-Range Weather Forecasts (ECMWF) Fifth-generation Reanalysis (ERA-5) data. The processing was conducted in PyAPS software (Jolivet et al., 2014). ~~Linear~~The phase ramps, which might be caused by residual tropospheric and ionospheric delays, were estimated by a 2-D quadratic model based on reliable pixels and removed from the displacement time series at each acquisition~~ using reliable pixels~~. The systematic topographic phase residuals caused by DEM errors were estimated based on the proportionality with the perpendicular baseline time series (Fattahi and Amelung, 2013). The processing described above was implemented by MintPy (Zhang et al., 2019b) ~~(https://github.com/insarlab/MintPy).~~(https://github.com/insarlab/MintPy).

Two indicators evaluated the quality of unwrapped phases and inverted raw phase time series: the phase closure of interferogram triplets and temporal coherence. The phase unwrapping algorithms add integer number of 2π phase jumps to recover the unwrapped phase. Interferometric phase noise and discontinuities among different coherent regions may lead to wrong 2π jumps added to the phase field known as unwrapping error. Unwrapping errors can bias the estimated time series. For an interferogram triplet ($\Delta\phi^{ij}$, $\Delta\phi^{jk}$ and $\Delta\phi^{ik}$), unwrapping errors introduce a nonzero integer component C_{int}^{ijk} in the closure phase C^{ijk}. Therefore, the number of interferogram triplets with nonzero integer ambiguity T_{int} can be used to detect unwrapping errors:

$$C^{ijk} = \Delta\varphi^{ij} + \Delta\varphi^{jk} - \Delta\varphi^{ik} \quad (2)$$

$$C_{int}^{ijk} = \frac{C^{ijk} - \mathrm{wrap}\,(C^{ijk})}{2\pi} \quad (3)$$

$$T_{int} = \sum_{i=1}^{T} \left(C_{int}^{ijk}\,! = 0\right) \quad (4)$$

where $\Delta\varphi^{ij}$, $\Delta\varphi^{jk}$ and $\Delta\varphi^{ik}$ are the three unwrapped interferometric phases generated from the SAR acquisitions at t_i, t_j and t_k, respectively; wrap is an operator that wraps each input number into $[-\pi, \pi)$; and T is the number of interferogram triplets. A triplet without unwrapping errors has $C_{int}^{ijk} \equiv 0$.

The second index, temporal coherence, represents the consistency of the time series with the network of interferograms (Pepe and Lanari, 2006):

$$\gamma_{\mathrm{temp}} = \frac{1}{M}\left|H^T \exp\,[j(\Delta\phi - A\hat{\phi})]\right| \quad (5)$$

where (for N SAR images and M interferograms) $\Delta\phi$ is the unwrapped interferometric phase; A is the $M \times (N-1)$ design matrix indicating the acquisition pairs used for interferograms generation (consisting of

-1, 0 and 1 for each row with -1 for the reference acquisition, 1 for the secondary acquisition and 0 for all other acquisitions (Berardino et al., 2002)); $\hat{\phi}$ denotes the estimated time series; H is an M×1 all-ones column vector; and j is the imaginary unit.

Temporal coherence varies from 0 to 1: pixels with values closer to 1 are considered reliable, whereas pixels with values closer to zero are considered unreliable. A threshold of 0.7 is recommended to be used for a dense network of interferograms. In this study, we used a threshold of 0.85; the pixels with temporal coherence below this threshold were masked from the final result.

iii) Reference point refinement and geocoding

In the natural environment,~~ the~~ exposed bedrock in flat terrain is normally selected as the reference point; however, because such exposed bedrock is scarce in the study area, we took great care in the selection of reference points. We selected a reference point ~~outside~~near the boundary of Selin Co watershed not affected by permafrost ~~region~~ in ~~very~~ dry and flat terrain. The residual phases from atmospheric distortions and tectonic movements on the TP are difficult to remove completely in such a large-scale extent. However, the effect could be reduced by setting the reference near the study area. The reference area was homogeneous and had interferometric coherence close to 1. Thus, we adjusted the displacements relative to this reference area~~.~~, the location of the reference area is marked in Fig. 1. Finally, we geocoded the deformation time series to the WGS84 coordinate system with ~~0.0005×0.0005 degree~~ a grid spacing of 0.0009°×0.0009° and then reprojected it ~~to~~onto the Albers equal area conic system with a 100 m×100 m grid size. To minimize the effects of extreme values, we also applied a 3-size moving window filtering to the deformation time series.

3.3.2 Extraction of ~~the~~ periodic (seasonal) ~~amplitude~~amplitudes and ~~long-term rate~~inter-annual deformation rates

The surface deformation in ~~the~~ permafrost terrain exhibits the characteristics of both long-term linear deformation and seasonal ~~oscillation (upheaval~~oscillations (uplift in winter and spring and subsidence in summer and autumn) (Daout et al., 2017; Li et al., 2015). ~~We used~~Therefore, we applied a sinusoidal (seasonal) function plus a linear (interannual) trend to the displacement time series of each image pixel using Eq. ~~(2). To minimize the effect of extreme values, we also applied a 3-size moving window filter to the deformation time series.~~(6).

$$d(t) = a \cdot t + A \cdot \sin\left(\frac{2\pi}{T} \cdot t + \varphi\right) + c \qquad (~~2~~6)$$

where t is the time interval with respect to the first SAR image acquisition date, a is the long-term deformation rate, A is the periodic (seasonal) amplitude, T is the period of the seasonal ~~undulations~~undulation (assumed to be one year), φ is the initial phase, and c is the residual term. a, A, φ and c are the coefficients to be determined. The peak-to-peak periodic (seasonal) deformation is twice the periodic amplitude of A. The seasonal amplitude shown in this work refers to the amount of A, not peak-to-peak deformation amount of 2A.

For each orbit, we extracted the LOS periodic (seasonal) amplitude and long-term deformation rate pixel by pixel from the deformation time series and then mosaiced the results from the two orbits together. The spatial grids of the incidence angles from the two orbits were mosaiced as well.

3.3.3 Deformation from the LOS ~~to vertical~~ direction to the vertical direction

For ~~the~~ flat terrain, deformation is caused mainly ~~caused~~ by freeze~~-~~–thaw cycles within the permafrost ~~activity~~layer and ~~is mainly~~occurs predominantly in the vertical direction. ~~Thus~~Hence, assuming no horizontal displacement, the observed deformation ~~is the terrain movement projection~~ in the line of the sight (LOS ~~direction. The observed deformation in the LOS~~) direction was converted ~~to~~into the vertical direction using Eq. (~~3~~7) by dividing the deformation value by the cosine of the incidence angle~~.~~ (the incidence angle ranges of orbit 48 and orbit 150 of the S1 ~~sensor~~satellites are listed in Table 1~~.~~):

$$d_v = d_{LOS}/\cos(\theta) \qquad (~~3~~7)$$

where d_{LOS} is the observed deformation along the ~~line of the sight~~LOS direction, d_v is the deformation in the vertical direction, and θ is the incidence angle of the sensor.

3.4 Conversion from ~~ground~~surface deformation ~~to~~into ground ice meltwater ~~contribution~~contributions

A considerable amount of ground ice is always buried in permafrost regions, especially just below the permafrost table~~; this ice forms mostly by ice segregation during the long permafrost formation process~~ (Cheng, 1983; Mackay, 1983; French and Harbor, 2013). Thawing of the uppermost permafrost layer is always accompanied by the compaction of sediment and subsidence of the ground surface due to the melting of super-saturated ground ice (French, 2017). Hence, the higher the ice content in permafrost ~~that melts under the warming climate~~, the larger the surface subsidence ~~that occurs~~occur as ~~a result.~~it was thawed. In this study, we assume that the cumulated long-term ~~subsided height in elevation~~settlement is equal to the thickness of ground ice ~~that melts.~~melted, and then release to the hydrological cycle. We converted the deformation rate into the ground ice meltwater via the following ~~these~~ steps:

i) Masking ~~off~~ areas with slope angles >10°

On steep slopes, ~~the~~ deformation occurs mainly as downslope movements driven by gravity (Buckel et al., 2021; Reinosch et al., 2020); thus, we considered only areas with slope angles below 10°. ~~The~~This threshold of 10° was adopted based on previous works (Reinosch et al., 2020; Buckel et al., 2021).

ii) Masking ~~off~~ areas with the LOS ~~direction~~ periodic (seasonal) amplitudes ≤1.5 mm or long-term velocities ≤2.5 mm/a

~~The threshold of 2.5 mm was~~These thresholds were similarly set based on previous works (Daout et al., 2017; Buckel et al., 2021)~~. A~~ and field surveys. The periodic seasonal threshold was used to mask ~~off~~ areas that ~~are not affected~~were unaffected by permafrost activity (because they do not experience periodic frost heave and thaw subsidence) but ~~exhibit~~exhibited continuous ~~sedimentary~~surface uplift or subsidence. Areas with periodic (seasonal) ~~oscillations in the amplitude~~ amplitudes below 1.5 mm and long-term (~~interannual~~inter-annual) velocities less than 2.5 mm are/a were likely unmoving considering distortions in the InSAR phase and DEM error.

iii) Conversion from groundsurface deformation into ground ice meltwater

SerlingSelin Co lake is located in the lowest area of the watershed, and the water released from thawing permafrost eventually enters the lake. The long-term deformation represents the elevation changes produced by the ground ice change. Using Eq. (48), by multiplying the grid cell size, we can obtain the ice volume change for each grid cell and then sum themamong all the cells to estimate the total ice volume amountcontribution. Because the density of water is ~1.0 g/cm^3 and that of ice is ~0.91 g/cm^3, the ice volume amount is then multiplied by a factor of 0.91 to convert to the corresponding water volume.:

$$\Delta V_{water} = 0.91 \cdot \Delta V_{ice} = 0.91 \cdot \sum \Delta h \cdot C_{grid} = 0.91 \cdot \sum d \cdot C_{grid} \quad (48)$$

where ΔV_{ice} is the change in the ground ice volume, Δh is the elevation change produced by the ice change, C_{grid} is the area of a grid cell, and d_v is the long-term deformation rate in the vertical direction.

4. Results

4.1 Lake water storage changechanges

We analyzed the lake storage changes in the lake water storage of three large lakes within the large SerlingSelin Co watershed: SerlingSelin Co, Ngoin Co, and the combination of Wuru Co & Qiagui Co. Fig.4 illustrates the time series of lake elevation of investigated lakes during October 2018 and 2020 derive by ICESat-2.Table 5 lists the surface extents and elevation changes of these three lakes are summarized in Table 5 and Table 6. From 2015 to 2020, Serlingof the investigated lakes on the Landsat acquisition dates. Selin Co expanded at a rate of 10.3 km^2/a from 2015 to 2020. Fig. . Limited by the data acquisition 4 illustrates the water surface elevation time series of the investigated lakes derived by ICESat-2 during October 2018 and 2020. During this period of ICESat-2, which was launched in 2018, we can confirm only that, the surface water increased at a rate of 0.2 m/a for Serling Co during 2018–2020. Calculated bySelin Co. Table 6 summarizes the averaged water surface elevation from each lake, considering all the elevation measurements within each year. The tracks of the elevation measurements in these years are plotted in Fig. 2(a-c). To calculate the changes in the lake area and height using Eq. (1), the lake water storage of Selin Co, Eq. (1) was applied taking the areas of 2408.1 km^2 in 2018 and 2441.2 km^2 in 2020 and taking the water surface elevation change of ~0.4 m between these two years; then, the change in lake volume from 2018 to 2020 increased by 496.3was estimated, and finally, the annual volume change rate was obtained by dividing the results of these two years. The annual rate of change in the lake volume of Selin Co during 2018–2020 was ~485×10^6 m^3/a.

Table 5 Lake areaareas from 2015 to 2020.

Lake	Area (km^2)

	2015	2016	2017	2018	2019	2020	Change ~~velocity~~rate (km²/a)
~~Serling~~Selin Co	2398.7	2377.1	2393.8	2408.1	2421.1	2441.2	10.3
Co Ngoin ~~Co~~	276.6	276.7	281.8	281.6	285.2	284.1	1.8
Wuru Co & Qiagui Co	432.5	437.2	432.5	452.5	447.2	443.0	2.9

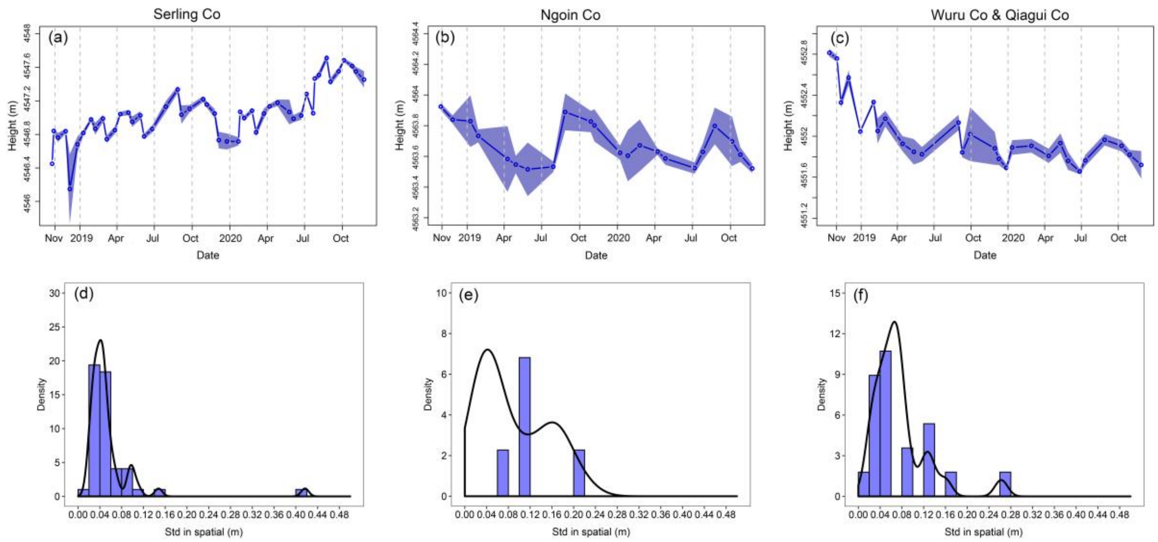

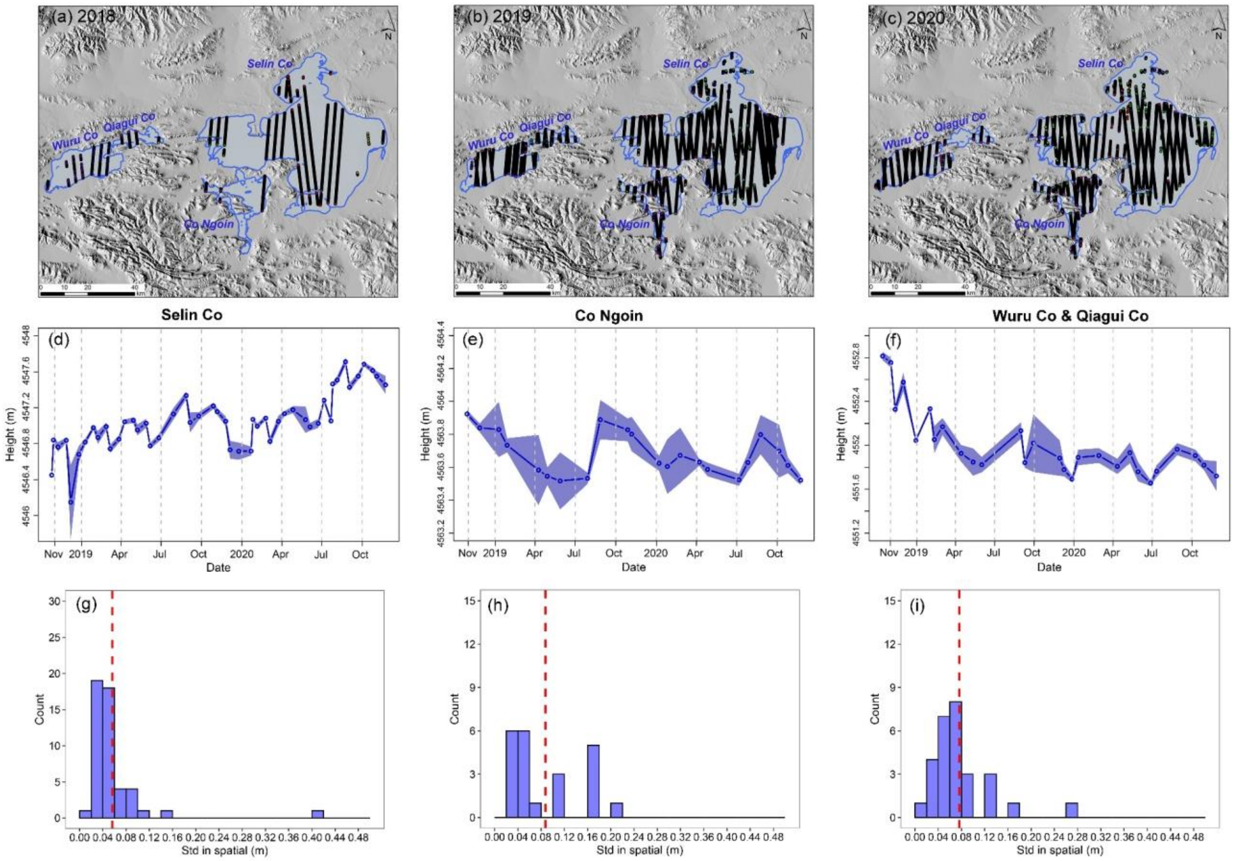

Figure 4 ~~Lake elevation from~~Water surface elevations of the three lakes. Subfigures (a)-(c) ~~are elevations derived from~~show tracks of the elevation measurements for each year. Subfigures (d)-(f) show the ICESat-2~~, in which~~ derived elevations. The solid lines indicate the average values of all elevation measurements within the lake on a given date~~, and~~. The light-colored areas show the mean ± one standard deviation. Subfigures (~~d)-(e~~g)-(i) further show ~~the~~ histograms of the standard ~~deviation~~deviations of the water surface elevation ~~within~~of the lake ~~of all acquisitions~~ from ~~2018 to 2020.~~ all acquisition dates. Red dashed line indicates the mean value.

~~**Table 6 Lake elevation from 2018 to 2020.**~~

Table 6 Lake elevations from 2018 to 2020, presented as the mean ± one standard deviation of all elevation measurements of the lake within the year. The tracks of the ICESat-2 elevation measurements are shown in Fig. 4 (a)-(c).

Lake	**Surface water elevation (m)**		
	2018	2019	2020
~~Serling~~Selin Co	4546.~~77~~72 ± 0.10	4546.~~99~~97 ± 0.17	4547.~~18~~20 ± 0.26
Ngoin Co	4563.~~85~~86 ± 0.05	4563.~~77~~74 ± 0.20	4563.~~68~~63 ± 0.14
Wuru Co & Qiagui Co	4552.~~50~~51 ± 0.26	~~4552.04~~4551.97 ± 0.20	4551.~~89~~87 ± 0.09

4.2 Ground surface deformation

4.2.1 Deformation at the borehole and GPR survey sites

The deformation time seriesFig. 5 shows the time series at five sites within a small (6.5 km × 6.5 km) region where the surface is flat and the elevation is lower than the Zhajiazangbu upstream region. For a better demonstration, this section is marked in Fig. 1. In this area, The mean annual air temperature is -2.0°C, calculated based on ERA5-Land air temperature hourly reanalysis data during 2017–2020. Sites 1–4 exhibit strong seasonal oscillations, whereas site 5 does not. As seen from Fig. 5(a), site 5 has almost no vegetation cover, and the surface is dry. The low water storage in the active layer explains its low seasonal amplitude because the seasonal deformation is mainly affected by the water content in the active layer due to the ice-water phase change in the active layer during the freeze-thaw cycle. Both subsidence and uplift signals are detected within the small extent of Fig. 5(a). The subsidence is the result of ground ice melting. The uplift signals of site 1 and site 4 are worth exploring. These signals might be related to ground ice aggradation; as shown in Fig. 5(a), they are very close to the streams, and A sufficient water supply accompanied by strong evaporation (cooling effect, energy is taken away) might facilitate the upward freezing of previously unfrozen (or seasonally frozen) sediment. Alternatively, the uplift signal might be related to alluvial sedimentation or groundwater table rise. However, in the area of Fig. 5(a), the uplift signal has a high possibility of being related to ground ice aggradation since the seasonal amplitude is very large. This phenomenon has been discussed by (Daout et al., 2020), who also found the coexistence of ground subsidence and uplift and speculated that excess meltwater pools and triggers an increase in segregation ice near the permafrost table.

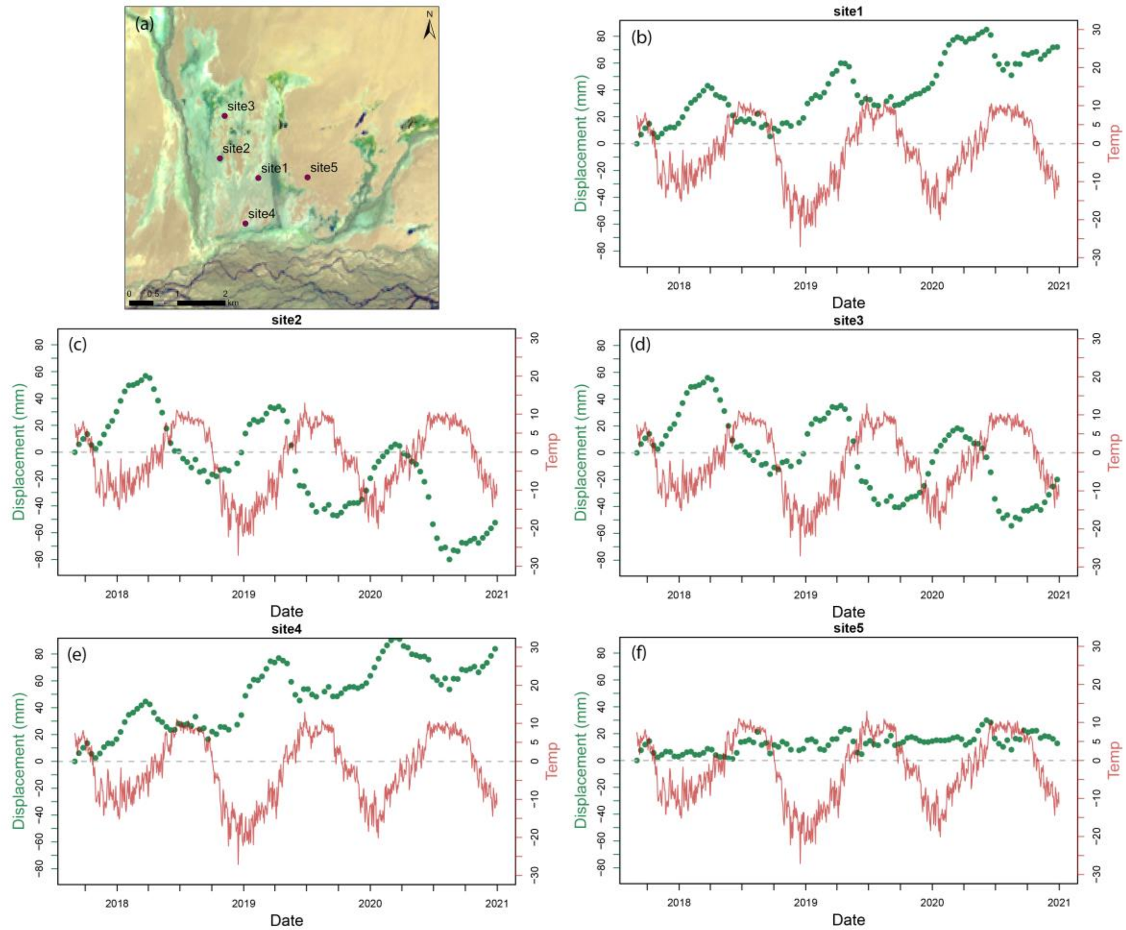

Figure 5 Deformation time series in the sector marked with the red rectangle in Fig. 1. Positive values represent uplift and negative values represent subsidence relative to the first scene of the S1 datasets. Air temperature in red color is from ERA5-Land air temperature hourly reanalysis data.

4.2.2 Spatial distributions of the seasonal amplitude and long-term rate

Fig. 6 and Fig. 7 show the spatial distributions of the long-term deformation rate and seasonal amplitude, respectively. The Serling Co basin spanned two orbits of Sentinel-1 images: orbit 48 and orbit 150. We extracted the seasonal and trend signals from the two orbits and mosaiced them together. The two results from orbit 150 and orbit 48 coincide with each other very well in the overlapping area, and we did not find any breaks or jumps in the place of stitching. This confirmed that the seasonal amplitudes and rate signals extracted from the two orbits are robust, although the acquisitions of the two orbits are not the same (Table 3).

The spatial distributions of both the seasonal amplitude and the long-term deformation rate are in accordance with the permafrost distribution map (Fig. 1). The boundary differentiating continuous permafrost from seasonally frozen ground in Fig. 1 exactly delineates the spatial distribution of the long-term deformation rate in Fig. 6 and that of the seasonal amplitude in Fig. 7. As shown in Fig. 6, widespread and large magnitudes of subsidence and large seasonal amplitudes are located in the upstream portion of the Zhajiazangbu subbasin southeast of Mt. Geladandong, where widespread continuous permafrost is present. Subsidence in the Serling Co watershed is normally between 5 and 20 mm/a (see the statistical details in Table 8) and reaches 50 mm/a in certain regions, reflecting high excess ice and rapid ice loss in the region. The seasonal amplitude ranges between 0 mm and 60 mm within the watershed area. Among the areas with velocities greater than 2.5 mm/a, 0.3% of them had seasonal amplitudes greater than 30 mm, 2.3% of them had amplitudes between 20 mm and 30 mm, 26.3% of them had amplitudes between 10 mm and 20 mm, 30.3% of them had amplitudes between 5 mm and 10 mm, and 40.9% of them had amplitudes of less than 5 mm; the average seasonal amplitude was 7.9 mm.

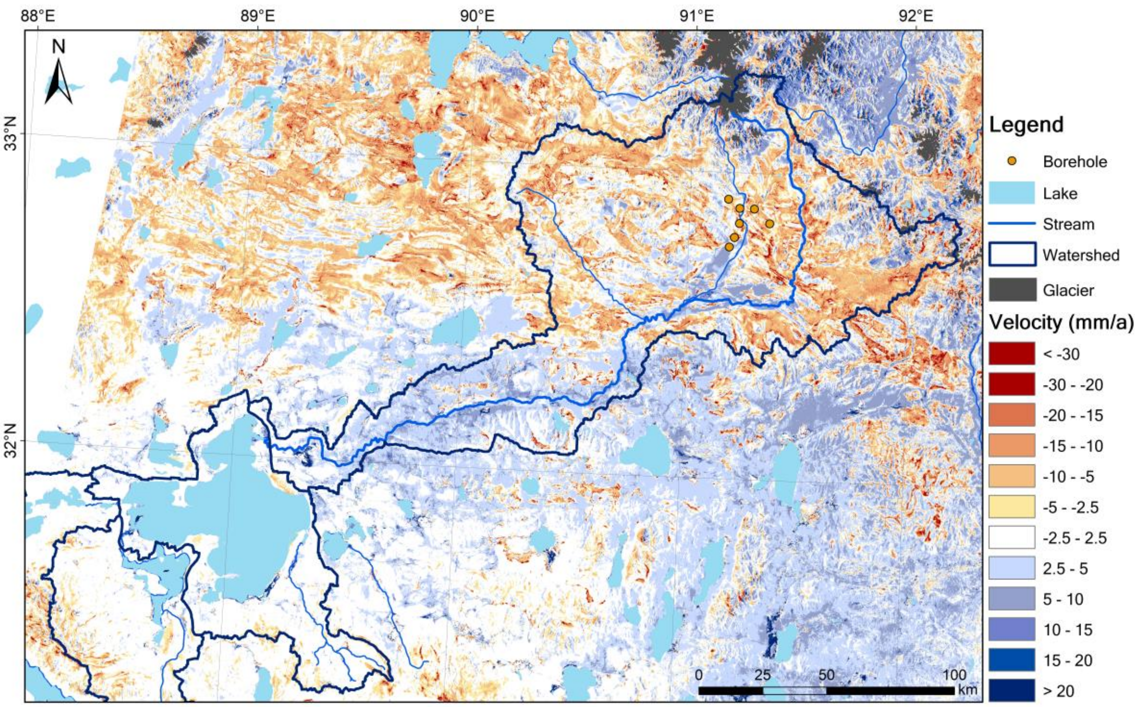

Figure 6 Map of the long-term deformation rate.

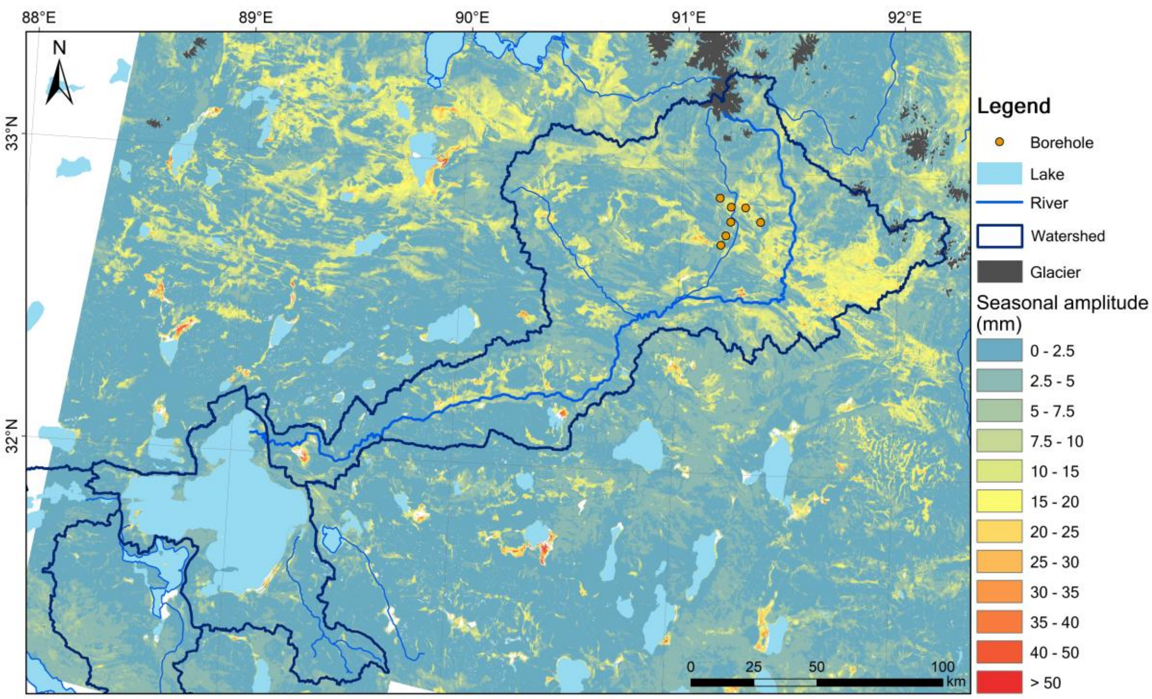

~~**Figure 7 Map of the periodic (seasonal) amplitude.**~~

~~4.2.3 Validation with GPR surveying and drilling sites~~ at the seven borehole sites are shown in Fig. 5.

~~We also examined the deformation characteristics at the GPR surveying and drilling sites. The deformation time series at seven drilling sites are shown in Fig. 8 and Table 7.~~ The detected deformation properties are highly consistent with the field surveys. Sites SLC03 and SLC04 ~~have~~displayed the largest seasonal amplitudes of 13.~~7~~8 mm and 16.~~5~~6 mm, respectively~~, and they~~; among all the borehole sites, these sites are the wettest and have the most developed vegetation cover, i.e., alpine swamp meadows with coverage higher than 90%. These seasonal amplitudes are to a large extent caused by the water~~-~~–ice phase changes in the freeze~~-~~–thaw cycle and are thus extremely sensitive to the water content in the active layer (Chen et al., 2020)~~.~~ ~~This sensitivity explains the high seasonal amplitudes at SLC03 and SLC04.~~. Permafrost can hold more water in the active layer than seasonally frozen ground; this is why site ~~SCL05 of~~SLC05 in seasonally frozen ground displayed the smallest seasonal oscillation of ~~1.9~~0.5 mm. ~~Similarly, among the twenty GPR segments where the existence of surface permafrost was confirmed, the seasonal amplitudes were all larger than 3.3 mm, with the largest amplitude of 19.9 mm and an average of 8.4 mm.~~

Excess ice was found in the SLC04 borehole; correspondingly, the largest subsidence velocity of ~~17.3~~18.9 mm/a was observed at this site. Likewise, SLC02~~, SLC03,~~ and SLC03, in which ground ice was found,~~ all~~ showed different levels of subsidence. Site SLC05, which is seasonally frozen and located in a river valley between two rivers, exhibited ~~a~~an uplift of ~~5.4~~3.2 mm/a, which might be because of sedimentation.

We also examined the deformation characteristics at the GPR

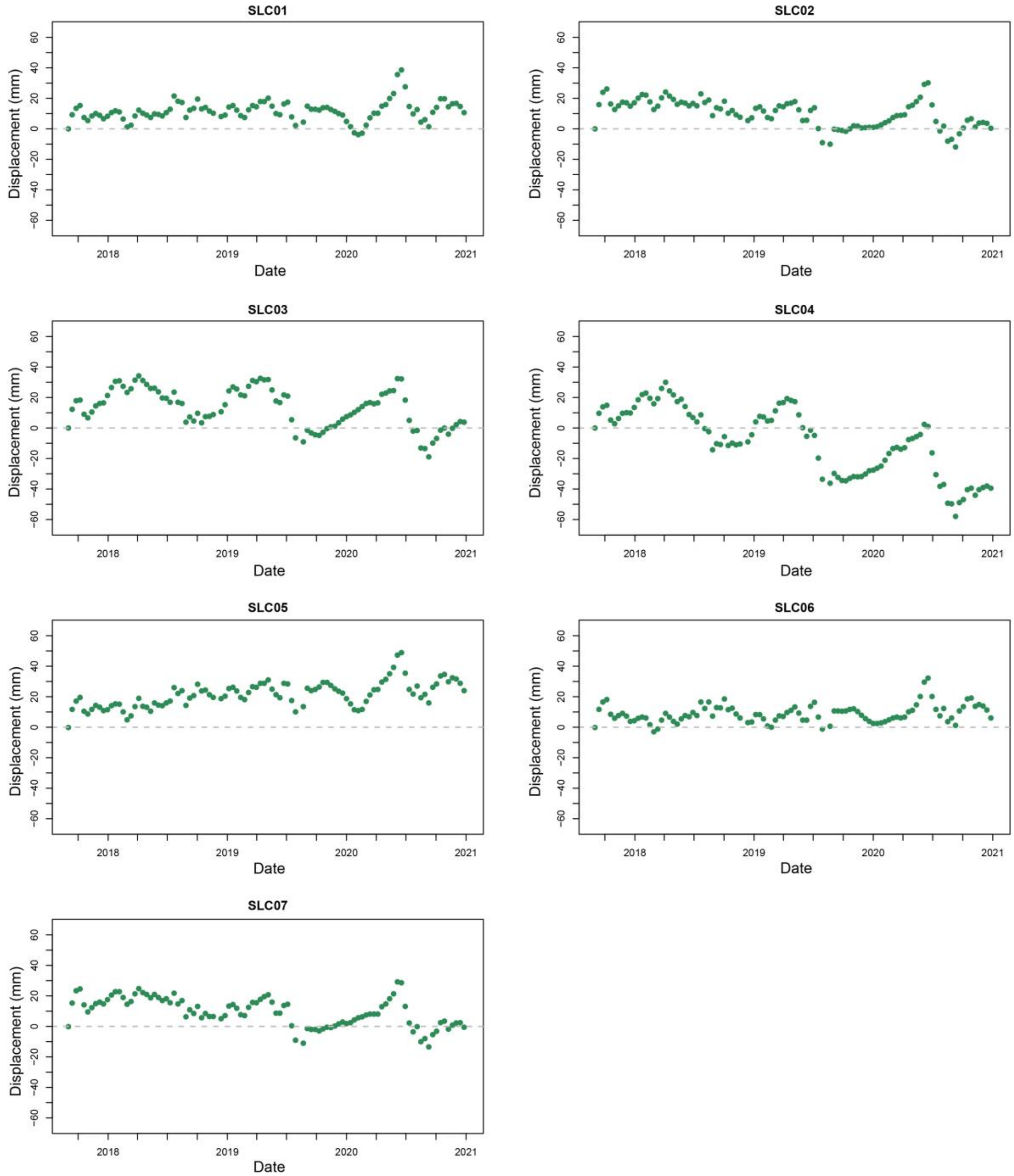

survey sites. Among the twenty GPR segments where permafrost existence was confirmed, the seasonal amplitudes were all larger than 2.0 mm, with a maximum amplitude of 16.2 mm and an average of 8.2 mm.

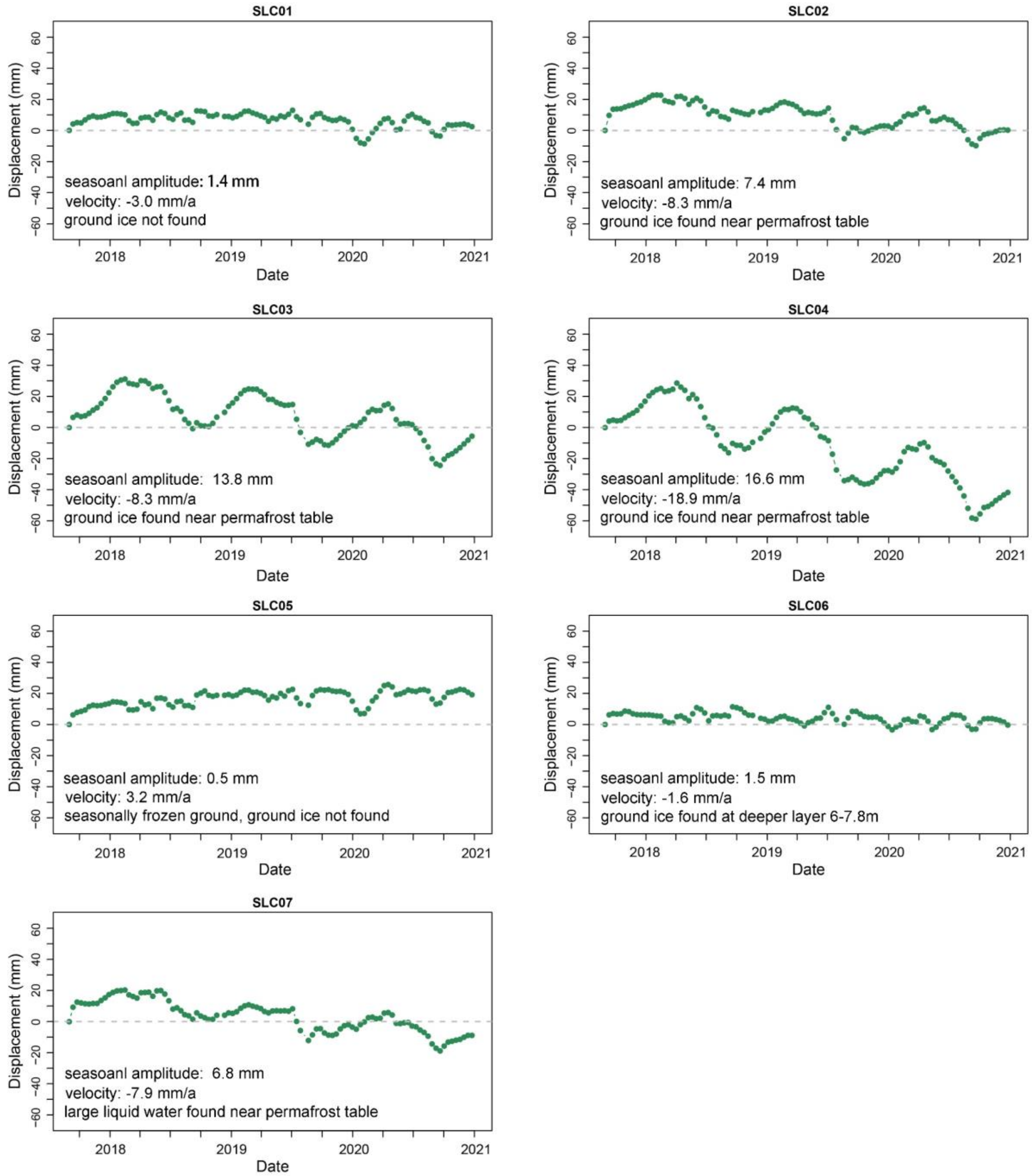

Figure ~~8~~5 LOS deformation time series at ~~seven drilling sites.~~

~~Table 7 Deformation properties at~~ the seven borehole sites. Positive values represent uplift and negative values represent subsidence relative to the first scene of the S1 datasets.

4.2.2 Spatial distributions of the	**~~Periodic seasonal oscillation (mm)~~**	**~~Deformation rate (mm/a)~~**

seasonal amplitude and long-term Site		
SLC01	3.0	1.4
SLC02	5.0	-5.1
SLC03	13.7	-5.6
SLC04	16.5	-17.3
SLC05	1.9	5.4
SLC06	3.5	1.5
SLC07	6.9	-5.4

deformation rate

Fig. 6 and Fig. 7 show the spatial distributions of the periodic (seasonal) amplitude and long-term (inter-annual) deformation rate, both of which are in accordance with the permafrost distribution map (Fig. 1). The boundary in Fig. 1 differentiating continuous permafrost from seasonally frozen ground exactly matches the boundaries observed for the seasonal amplitudes in Fig. 6 and the long-term deformation rates in Fig. 7. As shown in Fig. 6–7, widespread and large subsidence and large seasonal amplitudes are located in the upstream portion of the Zhajiazangbu subbasin southeast of Mt. Geladandong, where widespread continuous permafrost is present. Appendix Fig. A3 provides the deformation map covering the field investigation region.

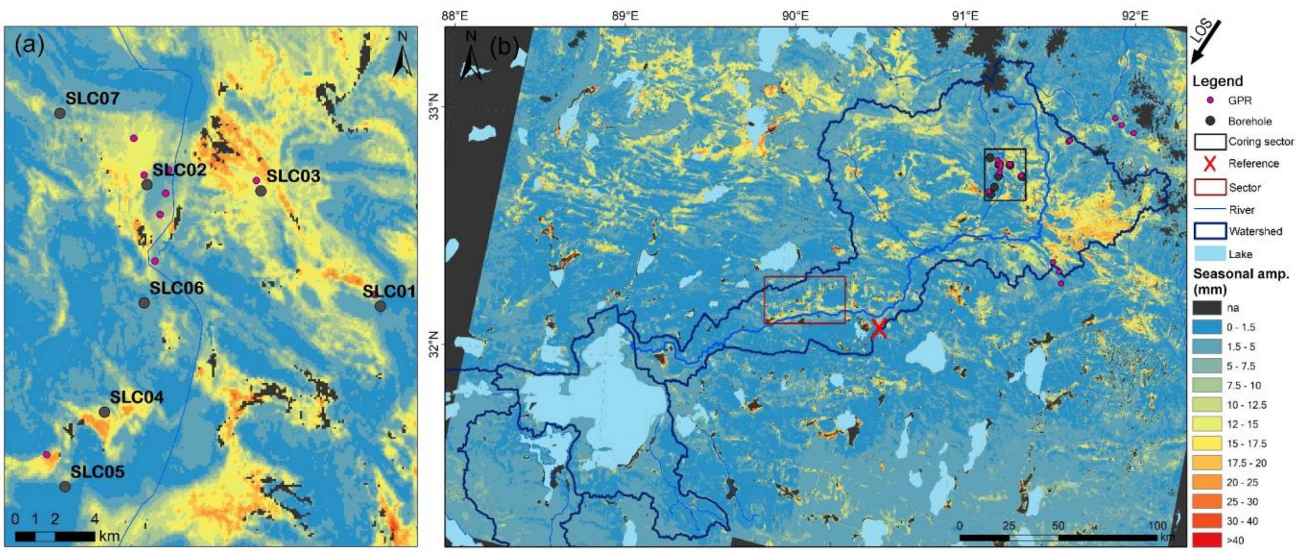

Figure 6 Map of the periodic (seasonal) amplitude in the satellite LOS direction. Subfigure (b) shows an enlarged view of the coring area (black sector in subfigure (a)). Dark grey colored "na" means the information could not be retrieved because of no data or decorrelation.

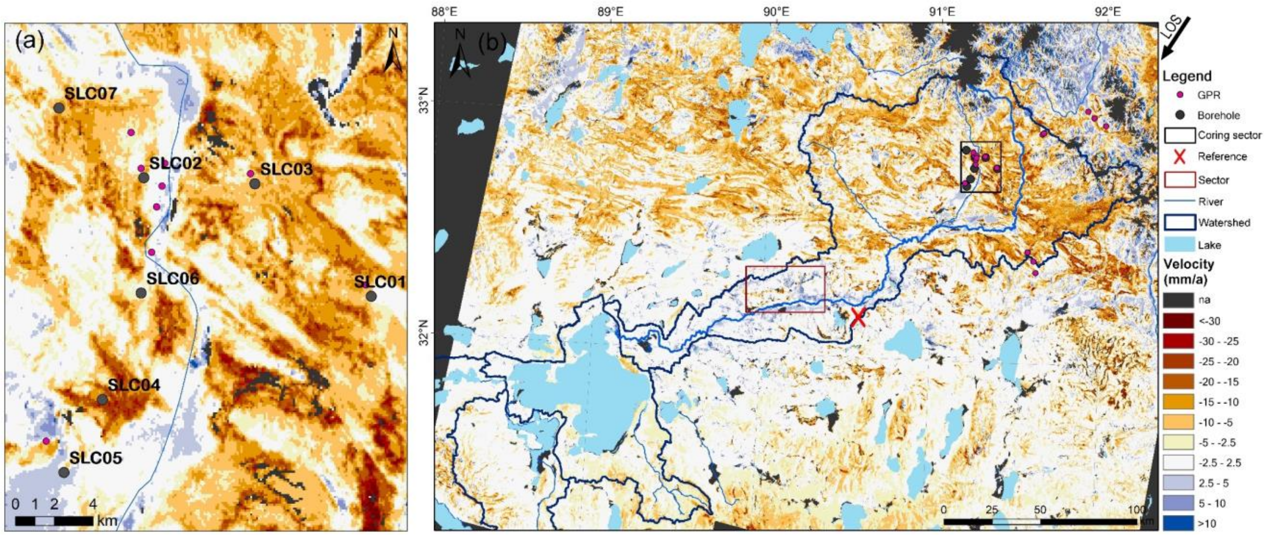

Figure 7 Map of the inter-annual deformation velocity in the satellite LOS direction. Subfigure (b) shows an enlarged view of the coring area (black sector in subfigure (a)). Dark grey colored “na” means the information could not be retrieved because of no data or decorrelation.

Fig. 8 shows a density plot of the seasonal amplitude versus the deformation rate. Subsidence in the Selin Co watershed was normally between 5 and 20 mm/a (see the statistical details in Table 8) but reached 50 mm/a in certain regions, reflecting highly excessive volumes of ice and rapid ice loss in this region. The seasonal amplitude ranged between 0 mm and 60 mm within the watershed area. In the Zhajiazangbu subbasin with extensive permafrost, among the areas with deformation rates greater than 2.5 mm/a, 0.1% of them had seasonal amplitudes greater than 30 mm, 2.2% had amplitudes between 20 mm and 30 mm, 24.1% had amplitudes between 10 mm and 20 mm, 23% had amplitudes between 5 mm and 10 mm, and 50.6% had amplitudes of less than 5 mm; overall, the average seasonal amplitude was 6.9 mm.

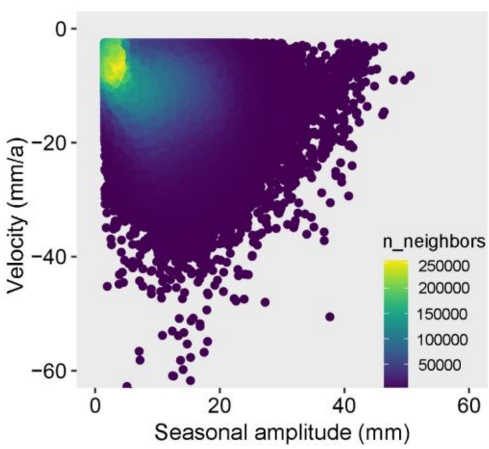

Figure 8 Distribution of the LOS seasonal amplitude versus the LOS deformation velocity within the Selin Co watershed, in all 6.57 ×10^5 valid pixels.

Table 8 Characteristics of terrain subsidence in the Selin Co basin.

Basin	Average (mm)	Percentage of subsidence (%)				
		-5 ~ -2.5 mm	-10 ~ -5 mm	-20 ~ -10 mm	-30 ~ -20 mm	< -30 mm
Zhajiazangbu subbasin	-10.6	13.8	36.7	44.3	4.9	0.3
Boquzangbu subbasin	-5.3	61.8	30.3	7.5	0.4	0
Overall	-10.3	16.3	36.3	42.3	4.7	0.3

4.3 Water ~~contribution from~~ contributed by ground ice melting

Fig. ~~Fig.~~ 9 shows ~~the~~a map of the potential volume of water ~~contribution caused~~contributed by changes in permafrost ground ice ~~change~~. Table 9 lists the statistics of the potential water contribution volume for the ~~Serling~~Selin Co basin. The main contribution comes from the Zhajiazangbu subbasin, where the permafrost coverage is 66.2%, ~~and~~whereas the contribution from the Boquzangbu subbasin is ~~very~~ limited. The potential rate ~~at which~~of ground ice meltwater ~~is generated~~generation was 55.~~4~~6×10^6 m^3/a in the Zhajiazangbu subbasin and ~~0.6~~1.9×10^6 m^3/a in the Boquzangbu subbasin, and the overall ~~amount is 56.0~~rate was 57.4×10^6 m^3/a. Compared to the ~~Serling Co~~ rate of change in the lake water storage ~~change velocity~~ of ~~496.3~~Selin Co (485×10^6 m^3/a~~,~~), we obtained a ground ice ~~melting water release~~meltwater contribution ratio of 11.~~3%. If~~8%. Converting the potential water contribution volume ~~is converted to~~ into the runoff depth ~~in~~within the watershed ~~extent, this value corresponds to~~yields a 2.~~6~~7 mm/a increase in the runoff depth.

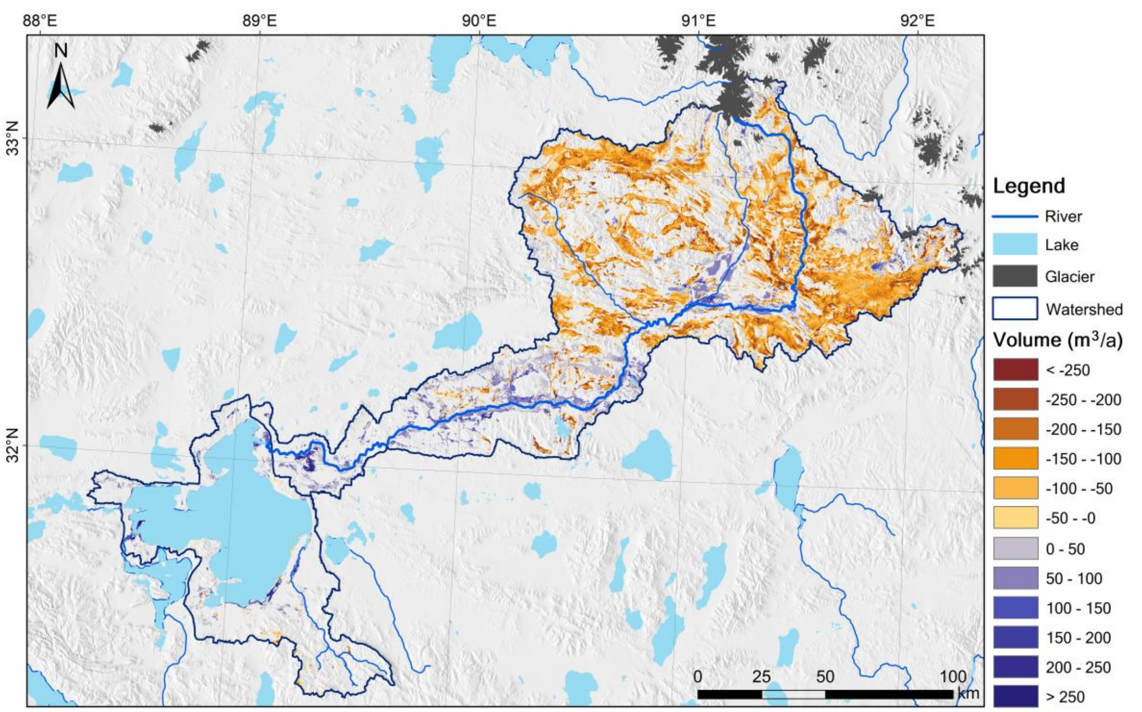

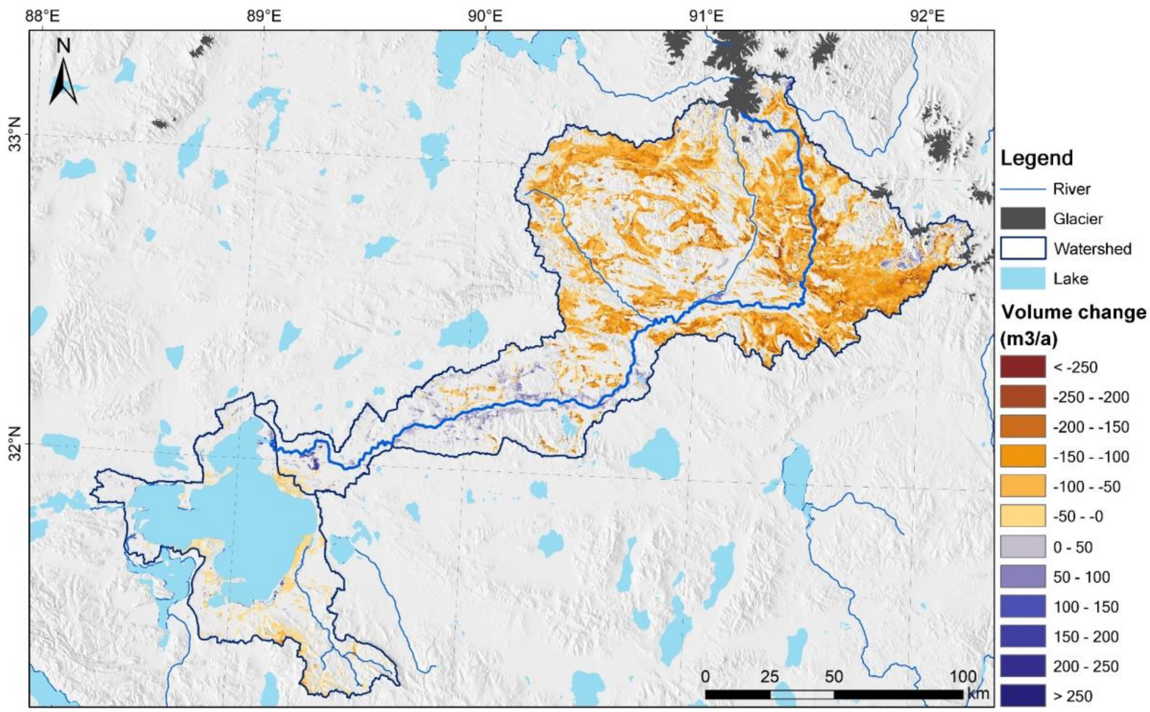

Figure 9 Map of the potential ~~water volume from~~ ground ice ~~change~~melting water supply. The grid color represents the ~~potential~~grid cell's yearly ground ice melting water ~~contribution~~supply volume ~~for the grid cell.~~, with negative values ~~indicate~~indicating ground ice loss and ~~water~~meltwater release.

~~We also considered two extreme situations when taking into account the ground surface uplift signals. If we assume all the uplift signals were caused by permafrost ground ice aggradation, thereby subtracting 14.6×10^6 m^3/a from 56.0×10^6 m^3/a, then a water contribution volume of 41.4×10^6 m^3/a is finally calculated and represents 8.3% of the lake water storage change. If the potential water contribution volume is converted into the runoff depth at the watershed scale, this value corresponds to a 1.9 mm/a increase in the runoff depth. If we assume all the uplift signals were caused by the rise of the groundwater table, which is recharged by melting of ground ice infiltration, then a water contribution volume of 70.6×10^6 m^3/a is finally calculated and represents 14.2% of the lake water storage change and a 3.3 mm/a increase in the runoff depth. Table 9 lists the water contribution of ground ice melting, as well as the extreme values when taking into account the signals of ground surface uplift.~~

Table 9 Yearly volume of ground ice meltwater contribution in the Selin Co watershed.

Basin	**Water volume (10^6 m^3/a)**	**Runoff depth (mm)**
Zhajiazangbu subbasin	55.6	3.5
Boquzangbu subbasin	1.9	0.3
Overall	57.4	2.7
Ratio of lake volume increasement	11.8%	

4.4 Uncertainty analysis

4.4.1 Uncertainties and accuracies of lake volume ~~change~~changes

Fig. 4(~~a~~d) clearly shows that the water surface elevation of ~~Serling~~Selin Co ~~lake is increasing~~has increased gradually, although ~~the~~ seasonal ~~fluctuation is~~fluctuations are evident as well. ~~Serling~~Selin Co ~~lake~~ has 49 ICESat-2 acquisitions ~~of ICESat-2 dataset~~ during the investigation period~~,~~ (Fig. 4(g)), and 69.4% of these acquisitions ~~has a standard deviation of~~correspond to elevation measurements with a standard deviation smaller than 0.05 m within the lake~~, as shown in Fig. 4(d). It~~. This means that the average values of all elevation measurements within the lake could represent the lake's elevation on a given date. To evaluate the accuracy of the resulting lake area extent, we validated the classification results by randomly selecting 1000 pixels ~~on~~from the Landsat images and visually ~~examined~~examining the classification results. ~~It shows that~~ The classification ~~accuracies reach around~~accuracy reached approximately 0.98.

~~Our analysis shows that during the period 2018–2020, the water level increased at a rate of 0.2 m/a, the lake area increased at a rate of 10.3 km^2/a, and the lake water storage increased at a rate of 496.3×10^6 m^3/a. These values were compared to the values recorded in previous studies. The water level remained stable during the period 1972–1999 and then increased at an approximate rate of 1.0 m/a in the period 2000–2006, after which the rate of increase gradually slowed down to 0.2 m/a during 2007–2011 (Doin et al., 2015). From 1972 to 2017, there was a 15.6 km^2/a increase in the lake area and a 425×10^6 m^3/a increase in the lake water storage, but the corresponding rates of increase in 1972–2000 were slow at 9.1 km^2/a and 368×10^6 m^3/a, respectively, and then they markedly accelerated in 2000–2005, with increases of 60.7 km^2/a and 1576×10^6 m^3/a, respectively; after that, in 2005–2017, the rates of increase in the lake area and water storage slowed to only 12.6 km^2/a and 553×10^6 m^3/a, respectively (Yang et al., 2017; Zhu et al., 2019). The values retrieved in this study are all in the range of historical values and closest to the values during the 2010s.~~

Our analysis shows that during the period of 2018–2020, the water level increased at a rate of ~0.2 m/a, the lake area increased at a rate of 10.3 km^2/a, and the lake water storage increased at a rate of 485×10^6 m^3/a. These values are compared with those recorded in previous studies in Fig. 10. Lake area change information are from (Zhu et al., 2019b; Qiao et al., 2019; Meng et al., 2012; Sun et al., 2020; Zhang et al., 2020; Deij et al., 2018); water level change information are from (Meng et al., 2012; Lei et al., 2013; Doin et al., 2015; Zhang et al., 2013; Sun et al., 2020; Hwang et al., 2019; Zhang et al., 2020; Zhu et al., 2019a); and water volume information are from (Zhu et al., 2019b; Qiao et al., 2019; Treichler et al., 2019; Sun et al., 2020; Zhang et al., 2013; Li et al., 2019). As illustrated in Fig. 10, the expansion of Selin Co was slow before 2000, with lake area and volume increases of 9.1 km^2/a and 368×10^6 m^3/a, respectively. Then, in the period of 2000–2005, the lake expanded extremely fast, with the water level increasing at an approximate rate of 1.0 m/a and the lake area and volume increasing at rates of 60.7 km^2/a and 1576×10^6 m^3/a, respectively. After 2005, however, these rates of increase slowed down, with those of the lake area and lake water storage slowing to only 12.6 km^2/a and 553×10^6 m^3/a during 2005–2017, respectively, and the rate of increase in the water surface elevation slowing to 0.2 m/a during 2007–2011 (Doin et al., 2015). Overall, the values retrieved in this study are all within the ranges of the historical values and are closest to the values after the 2010s.

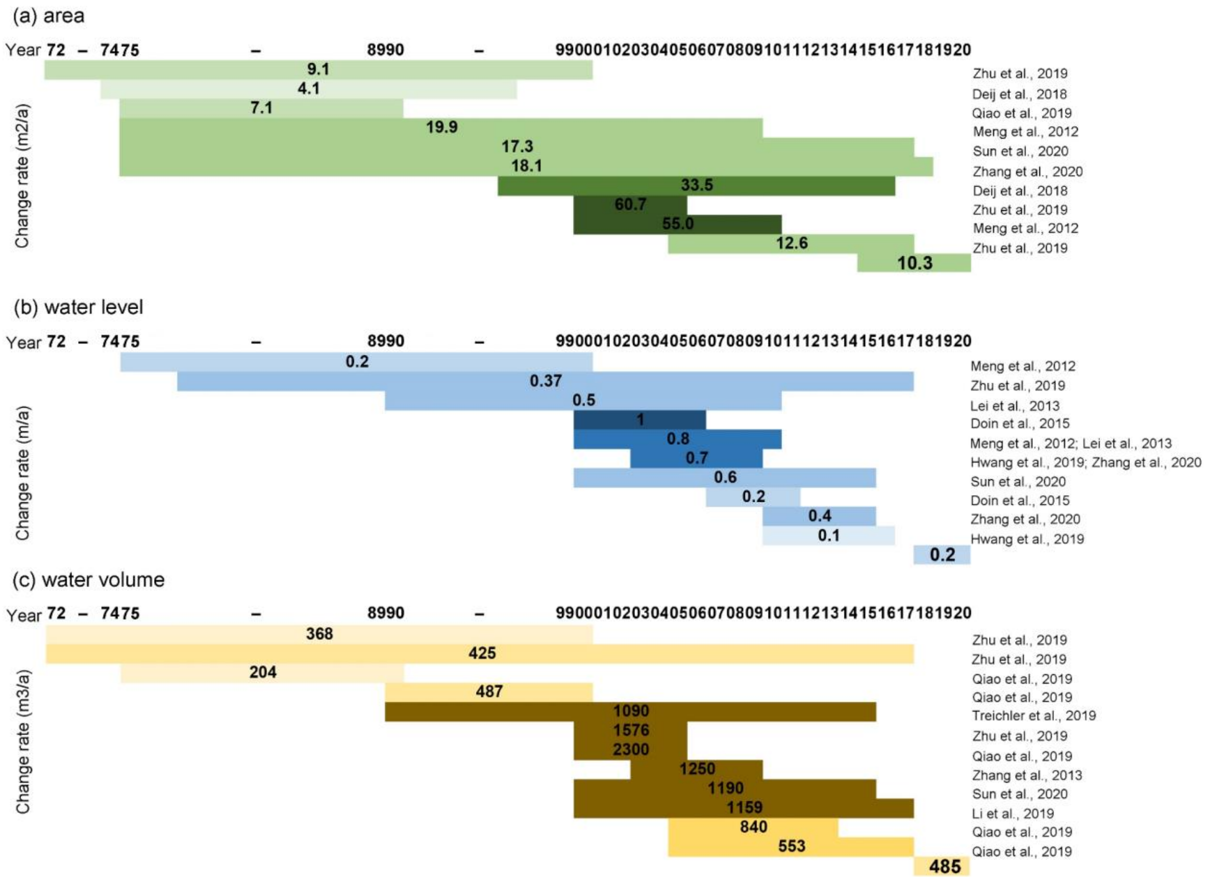

Figure 10 Comparisons of the changes in the lake area (subfigure a) water surface elevation (b) and lake volume (c) of Selin Co with historical values.

4.4.2 Uncertainties and accuracies of deformation

~~1) Uncertainties in long-term deformation velocity estimation~~

~~The standard deviation of the long-term deformation velocity parameter in Eq. (2) is applied to represent the uncertainties of the long-term deformation velocity estimation (Chen et al., 2018; Zhang et al., 2019b). Fig. 10 shows the standard deviation of the velocity estimator, 93.3% of the study area has a value less than 0.002 mm/a.~~

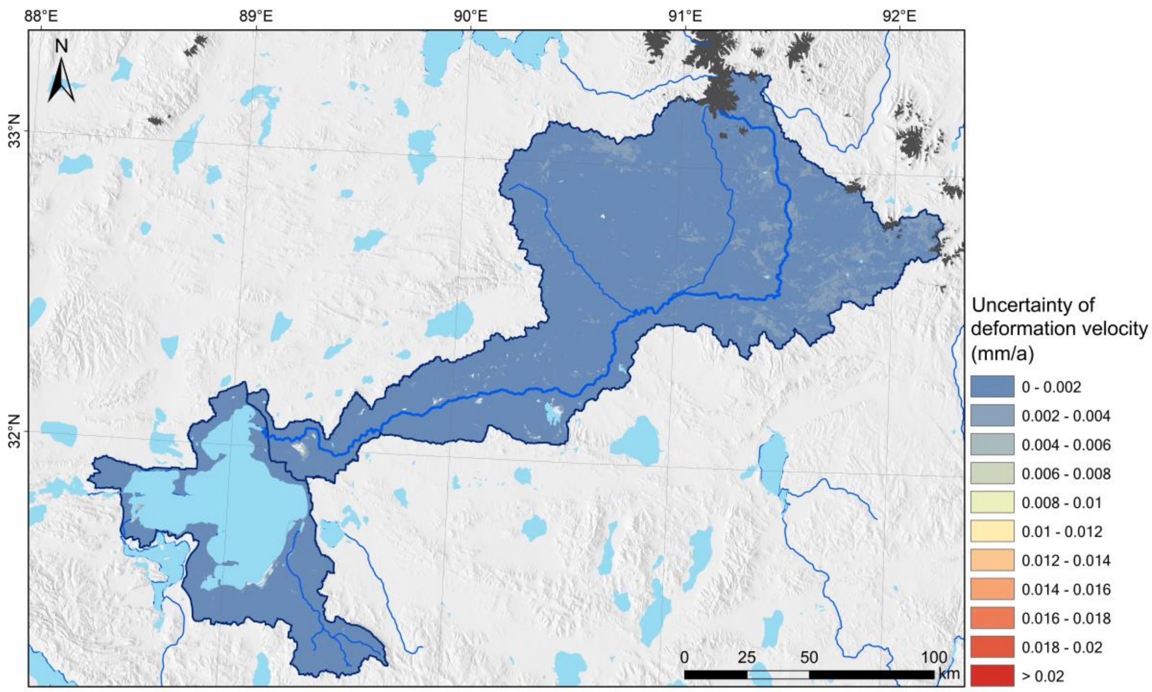

~~**Figure 10 Uncertainty of long-term deformation velocity.**~~

~~2) Accuracy of In-SAR derived deformation velocity~~

Two indicators evaluated the quality of unwrapped phases and inverted raw phase time series: the phase closure of interferogram triplets and temporal coherence. Fig. 11 shows the spatial distribution of the number of interferogram triplets with nonzero integer ambiguity T_{int} (Eq (4)), with the histogram illustrating the distribution of T_{int} values within the Selin Co watershed excluding glaciers and water bodies. The areas having T_{int} smaller than three take part 95% of the watershed, while 72.3% of the watershed has T_{int} value of zero (no wrapping error on all the interferograms). The T_{int} evaluated the quality of original interferometric unwrapped phases, the unwrapping errors could be further reduced by bridging reliable regions before network revision (Zhang et al., 2019b).

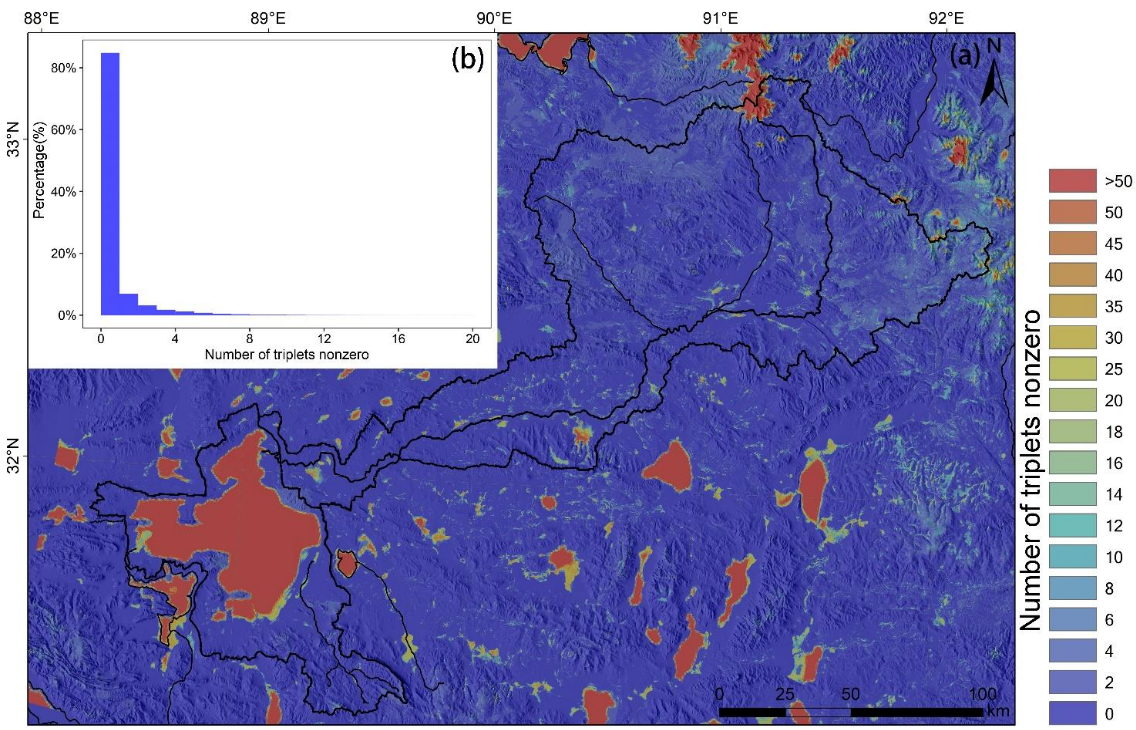

Figure 11 (a) Map of the number of interferogram triplets with nonzero integer ambiguity T_{int} (Eq(4)), (b) histogram illustrating the distribution of T_{int} values within the Selin Co watershed excluding glaciers and water bodies.

Fig. 12 shows the spatial distribution of temporal coherence (Eq. (5)), which is used to evaluate the quality of raw phase time series. 99.0% of the watershed has temporal coherence higher than 0.8, 98.1% has temporal coherence higher than 0.85, 96.0% has temporal coherence higher than 0.9 and 89.1% has temporal coherence higher than 0.95.

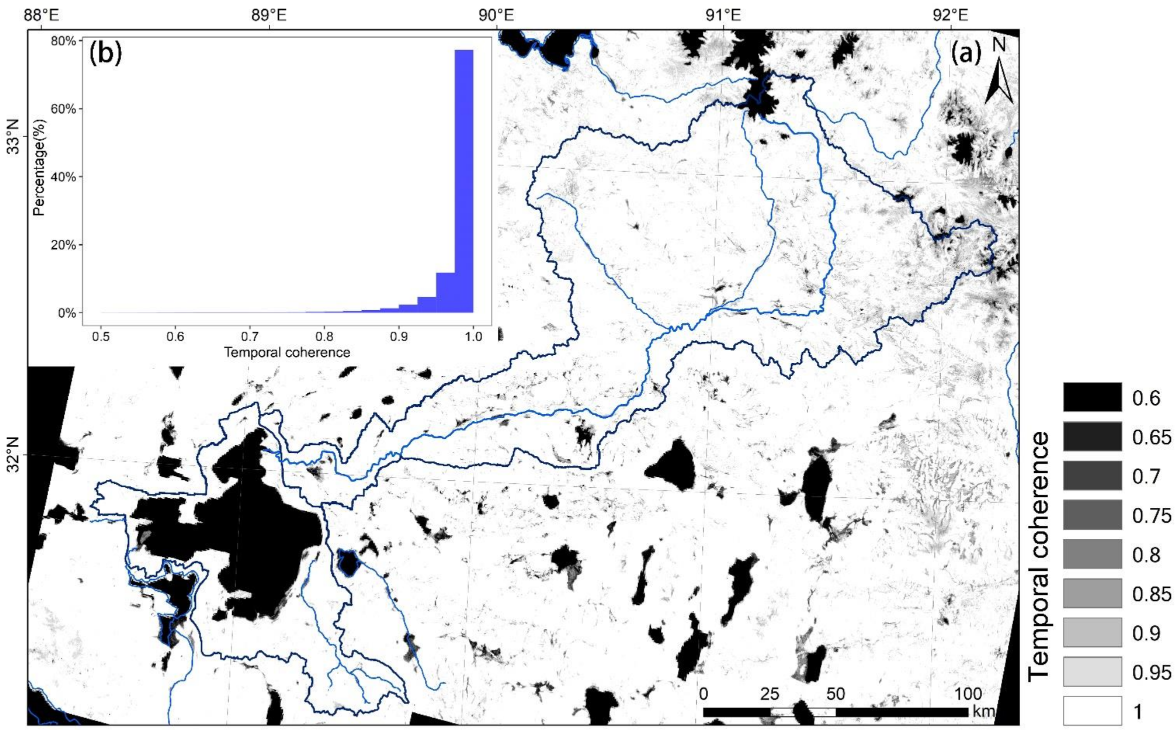

Figure 12 (a) Map of temporal coherence (Eq(5)), (b) histogram illustrating the distribution of temporal coherence values within the Selin Co watershed excluding glaciers and water bodies.

The Selin Co basin was covered by two orbits of S1 images: orbit 48 and orbit 150. Appendix Fig. A2 presents the amplitude and long-term velocity retrieved from orbit 48 and orbit 150, respectively. In the large overlapping area covering 270 km × 55 km, the results from orbit 150 and orbit 48 reveal identical deformation characters. This confirms that the seasonal amplitudes and deformation rates extracted from the two orbits are robust even though the acquisitions from the two orbits are not the same (Table 3).

In ~~this study~~addition, the deformation characteristics were compared with the ~~characteristics of~~observations from the boreholes, and excellent agreement was achieved. We also validated the SBAS-InSAR-derived deformation~~, –~~ (which has the same processing flow as applied in this study~~,~~) with the in situ leveling measurements at the Wudaoliang site on the ~~Tibetan Plateau~~TP; the relative error ~~is~~was found to be 14.8% regarding the long-term deformation rate (Zhou et al., 2019). Furthermore, we are currently ~~deploying~~operating an automatic deformation monitoring device in the watershed, and it is expected to provide an independent validation reference~~ in the watershed~~.

4.4.3 Uncertainties ~~of~~in the slope angle threshold in the estimation of ground ice meltwater ~~estimation~~

During the estimation process, we masked ~~out~~ regions with slopes steeper than the threshold of 10~~ degrees.~~°. We also tested the impact ~~on the results~~ of setting slope thresholds of 15~~ degrees~~° and 20~~ degrees.~~° on the results. When using the 15~~ degree~~° or 20° threshold~~ or the 20 degree threshold, the water release ~~, the volume of meltwater released changed by less than 1%. Hence, the setting of the threshold does not greatly influence the final ~~results~~prediction.

5. Discussion

5.1 Uplift displacement signal

In addition to widespread subsidence detected in the upstream of Zhajiazangbu of the continuous permafrost environment, the uplift signal was also observed in the sporadic permafrost environment in the middle stream of the Zhajiazangbu subbasin, also near some drained ponds. Fig. 13 shows a sector (location marked in red rectangle in Fig. 1, 6–7), in which both subsidence and uplift signals are detected. The mean annual air temperature is -2.0°C, calculated based on ERA5-Land air temperature hourly reanalysis data during 2017–2020. For a better interpretation, Landsat optical image and elevation with were also presented. The spatial distribution pattern of deformation aligns with landscape and topography very well. Large seasonal amplitude only appears in the vegetated and wet area, which indicates the water storage in the active layer in a certain way. Uplift signals are generally at the slope feet. Fig. 13(e)–(h) displays the deformation time series of four sites s1-s4 from high elevation to low elevation. Site s2 is stable, viewing from seasonal amplitude and long-term deformation velocity. The subsidence of site s3 is the result of ground ice melting, confirmed by the large periodic seasonal amplitude caused by frost heave and thaw subsidence in the active layer. The uplift signals of site s1 and site 4 are worth exploring, especially site s4. Site s4 has a possibility of being related to ground ice aggradation since it also exhibits moderate seasonal amplitude, but it is more likely related to sediment accumulation or groundwater table rise regarding its location.

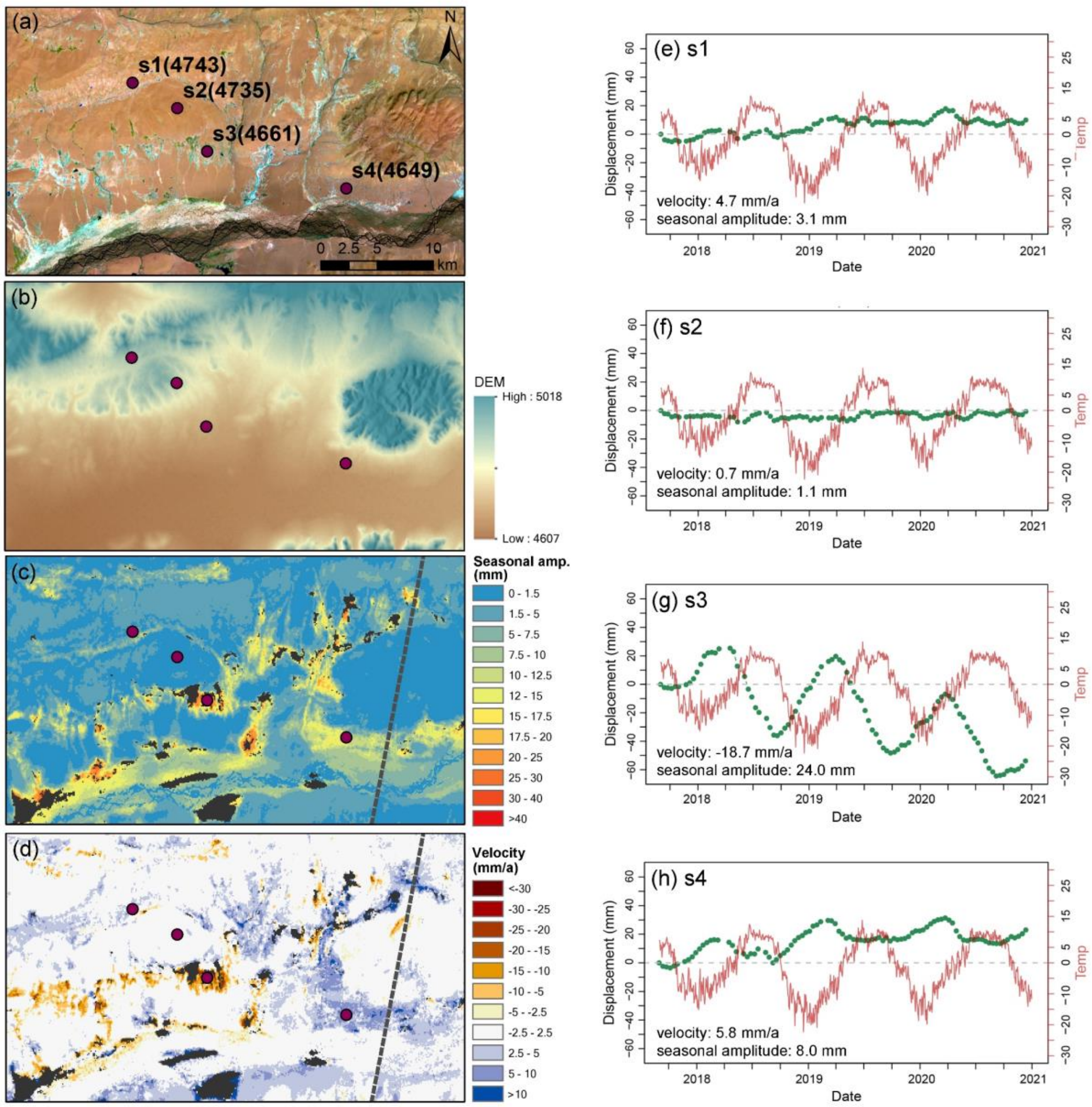

Figure 13 Deformation characters. This sector is marked with the red rectangle in Fig. 1 and 7-8. (a) Landsat 8 image (red: SWIR1, green: NIR, blue: red). (b) DEM overlapped on the hillshade, which is calculated using DEM with the Sentinel-1 incidence angle and azimuth angle. (c)(d) are seasonal deformation amplitude and long-term deformation velocity, respectively. The grey dashed line delineates the track boundary of orbit 150. (e)-(h) are deformation time series of marked sites. The elevetation (m a.s.l.) of the sites are labeled in brackets in subfigure (a). Air temperature in red color is from ERA5-Land air temperature reanalysis data. Deformations are in the LOS direction.

Previous research normally focuses on the thaw subsidence signal on the Tibetan PlateauTP, and less attention has been given to the uplift signal. Ground uplift was detected in the sporadic permafrost environment in the middle stream of the Zhajiazangbu subbasin and in some places around Serling Co lake, especially in drained ponds. It is also detected in the cold environment in the upstream portion of the Zhajiazangbu subbasin, where permafrost terrain is widely subsiding. Some of the uplift signals might be related to sedimentationdeposition or the rise of the groundwater table; in addition,. Some of thesethe uplift signals might be caused by ground ice aggradation. A sufficient water supply accompanied by strong evaporation (cooling effect, energy is taken away) might facilitate the upward freezing of previously unfrozen (or seasonally frozen) sediment. , as in these areas, the water supply is sufficient and the periodic seasonal deformation amplitude is large. Ground ice aggradation is slightly surprising in the overall warming climate of the study area. However, the upward freezing of previously unfrozen (or seasonally frozen) sediment is still possible and may occur because of sediment accretion (e.g., deltaic and alluvial sedimentation) (French, 2017). In our study area, the terrain uplift signals were found mainly near the rivers in a sedimentation landscape. A previous study (Daout et al., 2020) also detected a complex deformation signal in the permafrost on the northeastern Tibetan PlateauTP and hypothesized that the uplift deformation in lowland regions was caused by excess meltwater pooling, which triggered an increase in the segregation of ice near the permafrost table. Thus, on the Tibetan PlateauOn the TP, new permafrost forming is detected on the exposed bottom of Zonag Lake (Zhang et al., 2022). Thus, on the TP, it might be common for degradation and aggradation of ground ice to both occur in permafrost environments, with degradation representing the dominant pattern and aggradation existing in local areas. Currently, most studies focus on permafrost subsidence signals, and few studies have studied permafrost ground ice aggradation and the causes of uplift signals in local environments. Nevertheless, the uplift signals in the permafrost environment on the Tibetan PlateauTP are worthy of additional research, and further details on the SerlingSelin Co basin are expected to be unveiled and supplemented by the next field survey.

5.2 Water contribution fromby permafrost ground ice melting in the SerlingSelin Co watershed

In this study, we assumed that water the amount of surface settlement corresponds to the release of the same volume of ground ice as a result of compressing the thawing ice-rich permafrost layer and that the released by permafrost ice melt will water eventually enter Serlingenters Selin Co lake, and; the potential water contribution volume was estimated. accordingly. However, the effect of permafrost degradation on the terrestrial water cycle is complicated (Ma et al., 2020). TheA gradually thickening active layer may holdretain more water in the soil layer; thus, endorheic basins may collect more water during the thawing season. Additionally, the increase in the active layer thickness due to the warming climate could lead to moreenhanced evaporation. Furthermore, in permafrost terrain, the interactioninteractions between groundwater and surface water isare restricted. With continued permafrost degradation, the rates of groundwater recharge and discharge rates are expected to increase since the impermeable effect of barrier provided by permafrost weakens. Ultimately, the melting of ground ice can lead to the infiltration of more surface water infiltration into groundwater aquifers in the basin, resulting in an increase inthereby increasing groundwater storage in the basin (Bense et al., 2012; Zhang et al., 2017).

Based on the detected deformation, we estimated that the volumetric rate of water releasebeing released due to the melting of ground ice could reach 56.057.4×10^6 m^3/a for the Zhajiazangbu and Boquzangbu subbasins.

If the Alizangbu and Zhagenzangbu subbasins are included, the ~~permafrost thawing contribution amount~~volume contributed by ground ice melting could be even larger. According to the ~~statistics of~~ permafrost distribution statistics (Table 1), the Zhajiazangbu and Boquzangbu subbasins together have a permafrost area of 10791 km^2, ~~and~~while the other two subbasins, the Alizangbu and Zhagenzangbu, ~~together~~ have a combined permafrost area of only 2613 km^2, approximately ~~¼~~25% of the permafrost area in the two northern ~~two~~ subbasins. ~~According to~~ A map of the ground ice distribution on the ~~Tibetan Plateau,~~TP (Zhao and Sheng, 2019) likewise illustrates that the ground ice volumes in the Alizangbu and Zhagenzangbu subbasins are small compared to that in the Zhajiazangbu subbasin~~ (Zhao and Sheng, 2019). Moreover, the water released from ground ice melting does not directly supply Serling~~. Moreover, the water released from ground ice melting does not directly supply Selin Co in the Alizangbu and Zhagenzangbu subbasins; rather, this meltwater supplies Ngoin Co and Wuru Co & Qiagui Co first. In addition, during 2018–2020, the surface water level slightly dropped in Ngoin Co and Wuru Co & Qiagui Co (Fig. 4 and Table 5). Thus, the water supply from other lakes to ~~Serling~~Selin Co~~ lake~~ might be limited considering the circumstances stated above and thus was not ~~calculated~~incorporated into the calculation in the current study. In addition, there are some wet areas facing strong decorrelation (1.9% of watershed area has temporal decorrelation smaller than 0.85 and masked), where deformation information could not be retrieved. However, these areas usually experience very large subsidence. If taking into account of these areas, the ground ice meltwater contribution could be higher. If only the retrieved subsidence signal is considered, the ground ice meltwater volume contribution is ~~55.6~~57.4×10^6 m^3/a, accounting for 11.~~2~~8% of the lake volume increase. ~~The~~This result is consistent with a previous model simulation of the ~~Tibetan Plateau's~~ water supply of permafrost degradation to the lake volume increase of the endorheic basins on the TP (Zhang et al., 2017), which ~~found~~estimated the water supply by multiplying the active layer thickening rate and the average ground ice content and revealed that permafrost degradation contributed ~12% of the water supply to the lake volume increase~~. Our deformation-based estimation could confirm that the contribution of ground ice meltwater could reach 10% in the study period of 2017–2020~~.

Our ~~3~~three-year study period is relatively short compared to the continuous period of the growth of ~~Serling~~Selin Co from the 1970s to the present. The deformation rate and the lake water storage increasing rate in the other periods might be different from those in 2017–2020. C-band ERS, ENVISAT, and L-band ALOS PALSAR provide historical SAR data from the 1990s to the 2010s and will be processed and analyzed in a future study.

6. Conclusions

This is the first study to quantify the contribution of ground ice ~~change~~melting to the expansion of ~~Serling~~Selin Co~~ lake~~. We monitored the surface deformation using the SBAS-InSAR technique over a large area of approximately 450 km~~ × ~~×500 km across the ~~Serling~~Selin Co~~ lake~~ basin and then utilized the long-term deformation ~~rate~~rates to estimate the potential ~~amount~~volume of water being released ~~from~~via ground ice melting. Then, this amount was compared with the lake volume change during the same period, and the contribution ratio was derived. SBAS-InSAR monitoring during 2017–2020 ~~illustrated~~exposed widespread and large subsidence in the upstream section of the Zhajiazangbu subbasin, ~~where~~which is underlain by widespread, continuous permafrost~~ is present. The subsidence was~~. Subsidence normally occurred between 5 and 20 mm/a (~~72.8~~78.6%), indicating ~~high~~highly excess ice and rapid ice loss in the region. During the same period, the lake water storage increased at a rate of approximately ~~496.3~~485×10^6 m^3/a, and the potential rate ~~of~~at which water ~~release from~~was being released due to ground ice melting reached ~~56.0~~57.4×10^6 m^3/a, contributing 11.~~3~~8% of the lake volume increase. The uplift signals in some lowland areas with a sufficient water supply and in drained ponds are worth noting, and more details will be revealed through future field surveys. This study is especially helpful ~~in~~for explaining the rapid expansion of ~~Serling~~Selin Co~~ lake~~ and equilibrating the water balance at the watershed scale. More importantly, the proposed method can be easily extended to other watersheds underlain by permafrost ~~and can~~to help us better understand the ~~hydrologic~~hydrological changes in these watersheds.

Acknowledgments

This work was supported by research grants from the National Natural Science Foundation of China (No. 42001054 and 41931180), the Second Tibetan Plateau Scientific Expedition and Research (STEP) program (No. 2019QZKK0201), and the Natural Science Foundation of the Jiangsu Province (BK20200828). We are also grateful to the logistics staff who provided tremendous help during the field campaign.

Data availability

Sentinel-1 Level 1 single-look complex (SLC) images can be accessed from the Alaska Satellite Facility (https://search.asf.alaska.edu/) or Copernicus Open Access Hub (https://scihub.copernicus.eu/). The lake area extents during 2015–2017 were from the datasets "The lakes larger than 1km^2 in Tibetan Plateau (V2.0)", provided by the National Tibetan Plateau Data Center.

Author contribution

L. Wang and L. Zhao designed the study and wrote the manuscript. L. Zhao directed the project. L. Wang, H. Zhou, S. Liu, and C. Li performed the surface deformation analysis; X. Li performed the lake water level analysis; E. Du conducted GPR survey and interpretation; L. Zhao, G. Liu, D. Zou, H. Zhou, Z. Sun, E. Du, Y. Xiao, G. Hu, S. Liu, Z. Li, C. Wang, Y Qiao and T. Wu conducted the field works and borehole drillings. L. Wang, L. Zhao, H. Zhou, S. Liu, D. Zou, G. Liu, E. Du interpreted and discussed the results.

Competing interests

No conflict of interest.

References

Bense, V., Kooi, H., Ferguson, G., and Read, T.: Permafrost degradation as a control on hydrogeological regime shifts in a warming climate, Journal of Geophysical Research: Earth Surface, 117, 2012.

Berardino, P., Fornaro, G., Lanari, R., and Sansosti, E.: A new algorithm for surface deformation monitoring based on small baseline differential SAR interferograms, Geoscience and Remote Sensing, IEEE Transactions on, 40, 2375-2383, 2002.

Bian, D., Bian, B., La, B., Wang, C., and Chen, T.: The Response of Water Level of Selin Co to Climate Change during 1975-2008 (in Chinese), ~~Journal of Geographical Sciences, 65, 313-319~~Acta Geographica Sinica, 65, 2010.

Brun, F., Treichler, D., Shean, D., and Immerzeel, W. W.: Limited contribution of glacier mass loss to the recent increase in Tibetan Plateau lake volume, Frontiers in Earth Science, 8, 495, 2020.

Buckel, J., Reinosch, E., Hördt, A., Zhang, F., Riedel, B., Gerke, M., Schwalb, A., and Mäusbacher, R.: Insights into a remote cryosphere: a multi-method approach to assess permafrost occurrence at the Qugaqie basin, western Nyainqêntanglha Range, Tibetan Plateau, The Cryosphere, 15, 149-168, 2021.

Chen, C. W. and Zebker, H. A.: Phase unwrapping for large SAR interferograms: Statistical segmentation and generalized network models, IEEE Transactions on Geoscience and Remote Sensing, 40, 1709-1719, 2002.

Chen, J., Liu, L., Zhang, T., Cao, B., and Lin, H.: Using persistent scatterer interferometry to map and quantify permafrost thaw subsidence: A case study of Eboling Mountain on the Qinghai‐Tibet Plateau, Journal of Geophysical Research: Earth Surface, 123, 2663-2676, 2018.

Chen, J., Wu, Y., O'Connor, M., Cardenas, M. B., Schaefer, K., Michaelides, R., and Kling, G.: Active layer freeze-thaw and water storage dynamics in permafrost environments inferred from InSAR, Remote Sensing of Environment, 248, 112007, 2020.

Chen, J., Wu, T., Zou, D., Liu, L., Wu, X., Gong, W., Zhu, X., Li, R., Hao, J., and Hu, G.: Magnitudes and patterns of large-scale permafrost ground deformation revealed by Sentinel-1 InSAR on the central Qinghai-Tibet Plateau, Remote Sensing of Environment, 268, 112778, 2022.

Cheng, G.: The mechanism of repeated-segregation for the formation of thick layered ground ice, Cold Regions Science and Technology, 8, 57-66, 1983.

Daout, S., Dini, B., Haeberli, W., Doin, M.-P., and Parsons, B.: Ice loss in the Northeastern Tibetan Plateau permafrost as seen by 16 yr of ESA SAR missions, Earth and Planetary Science Letters, 545, 116404, 2020.

Daout, S., Doin, M. P., Peltzer, G., Socquet, A., and Lasserre, C.: Large‐scale InSAR monitoring of permafrost freeze‐thaw cycles on the Tibetan Plateau, Geophysical Research Letters, 44, 901-909, 2017.

Deij, Y., Nima, J., Qianba, O., Zeng, L., and Luosang, Q.: Lake Area Variation of Selin Tso in 1975 ~ 2016 and Its Influential Factors, Plateau and Mountain Meteorology Research, 38, 2018.

Doin, M. P., Twardzik, C., Ducret, G., Lasserre, C., Guillaso, S., and Jianbao, S.: InSAR measurement of the deformation around Siling Co Lake: Inferences on the lower crust viscosity in central Tibet, Journal of Geophysical Research: Solid Earth, 120, 5290-5310, 2015.

Farinotti, D., Huss, M., Fürst, J. J., Landmann, J., Machguth, H., Maussion, F., and Pandit, A.: A consensus estimate for the ice thickness distribution of all glaciers on Earth, Nature Geoscience, 12, 168-173, 2019.

Fattahi, H. and Amelung, F.: DEM error correction in InSAR time series, IEEE Transactions on Geoscience and Remote Sensing, 51, 4249-4259, 2013.

French, H. and Harbor, J.: 8.1 The Development and History of Glacial and Periglacial Geomorphology, Treatise on Geomorphology, Academic Press, https://doi.org/10.1016/B978-0-12-374739-6.00190-1, 2013.

French, H. M.: The periglacial environment, John Wiley & Sons2017.

~~Guarnieri, A. M. and Tebaldini, S.: On the exploitation of target statistics for SAR interferometry applications, IEEE Transactions on Geoscience and Remote Sensing, 46, 3436-3443, 2008.~~

Günther, F., Overduin, P. P., Yakshina, I. A., Opel, T., Baranskaya, A. V., and Grigoriev, M. N.: Observing Muostakh disappear: permafrost thaw subsidence and erosion of a ground-ice-rich island in response to arctic summer warming and sea ice reduction, The Cryosphere, 9, 151-178, 2015.

Guo, W., Liu, S., Xu, J., Wu, L., Shangguan, D., Yao, X., Wei, J., Bao, W., Yu, P., and Liu, Q.: The second Chinese glacier inventory: data, methods and results, Journal of Glaciology, 61, 357-372, 2015.

Guo, Y., Zhang, Y., Ma, N., Xu, J., and Zhang, T.: Long-term changes in evaporation over Siling Co Lake on the Tibetan Plateau and its impact on recent rapid lake expansion, Atmospheric research, 216, 141-150, 2019.

Hwang, C.-w., Cheng, Y. S., Yang, W. H., Zhang, G., Huang, Y. R., Shen, W. B., and Pan, Y.: Lake level changes in the Tibetan Plateau from Cryosat-2, SARAL, ICESat, and Jason-2 altimeters, Terr. Atmos. Ocean. Sci, 30, 1-18, 2019.

Jin, H., Huang, Y., Bense, V. F., Ma, Q., Marchenko, S. S., Shepelev, V. V., Hu, Y., Liang, S., Spektor, V. V., and Jin, X.: Permafrost Degradation and Its Hydrogeological Impacts, Water, 14, 372, 2022.

Jolivet, R., Agram, P. S., Lin, N. Y., Simons, M., Doin, M. P., Peltzer, G., and Li, Z.: Improving InSAR geodesy using global atmospheric models, Journal of Geophysical Research: Solid Earth, 119, 2324-2341, 2014.

Kokelj, S. V. and Jorgenson, M.: Advances in thermokarst research, Permafrost and Periglacial Processes, 24, 108-119, 2013.

Lanari, R., Lundgren, P., Manzo, M., and Casu, F.: Satellite radar interferometry time series analysis of surface deformation for Los Angeles, California, Geophysical Research Letters, 31, 2004.

Lantuit, H. and Pollard, W.: Fifty years of coastal erosion and retrogressive thaw slump activity on Herschel Island, southern Beaufort Sea, Yukon Territory, Canada, Geomorphology, 95, 84-102, 2008.

Lei, Y., Yao, T., Bird, B. W., Yang, K., Zhai, J., and Sheng, Y.: Coherent lake growth on the central Tibetan Plateau since the 1970s: Characterization and attribution, Journal of Hydrology, 483, 61-67, 2013.

Lei, Y., Yang, K., Wang, B., Sheng, Y., Bird, B. W., Zhang, G., and Tian, L.: Response of inland lake dynamics over the Tibetan Plateau to climate change, Climatic Change, 125, 281-290, 2014.

Li, X., Long, D., Huang, Q., Han, P., Zhao, F., and Wada, Y.: High-temporal-resolution water level and storage change data sets for lakes on the Tibetan Plateau during 2000–2017 using multiple altimetric missions and Landsat-derived lake shoreline positions, Earth System Science Data, 11, 1603-1627, 2019.

Li, Y., Liao, J., Guo, H., Liu, Z., and Shen, G.: Patterns and potential drivers of dramatic changes in Tibetan lakes, 1972–2010, PloS one, 9, e111890, 2014.

Li, Z., Zhao, R., Hu, J., Wen, L., Feng, G., Zhang, Z., and Wang, Q.: InSAR analysis of surface deformation over permafrost to estimate active layer thickness based on one-dimensional heat transfer model of soils, Scientific reports, 5, 2015.

Liu, L., Schaefer, K., Zhang, T., and Wahr, J.: Estimating 1992–2000 average active layer thickness on the Alaskan North Slope from remotely sensed surface subsidence, Journal of Geophysical Research: Earth Surface, 117, ~~2012~~2012a.

Liu, S., Guo, W., and Xu, J.: The second glacier inventory dataset of China (version 1.0) (2006-2011) [dataset], 10.3972/glacier.001.2013.db, 2012b.

Lu, P., Han, J., Li, Z., Xu, R., Li, R., Hao, T., and Qiao, G.: Lake outburst accelerated permafrost degradation on Qinghai-Tibet Plateau, Remote Sensing of Environment, 249, 112011, 2020.

Ma, Q., Jin, H.-J., Bense, V. F., Dong-Liang, L., Marchenko, S. S., Harris, S. A., and Lan, Y.-C.: Impacts of degrading permafrost on streamflow in the source area of Yellow River on the Qinghai-Tibet Plateau, China, Advances in Climate Change Research, 2020.

Mackay, J. R.: Downward water movement into frozen ground, western arctic coast, Canada, Canadian Journal of Earth Sciences, 20, 120-134, 1983.

Meng, K., Shi, X., Wang, E., and Liu, F.: High-altitude salt lake elevation changes and glacial ablation in Central Tibet, 2000–2010, Chinese Science Bulletin, 57, 525-534, 2012.

Pepe, A. and Lanari, R.: On the extension of the minimum cost flow algorithm for phase unwrapping of multitemporal differential SAR interferograms, IEEE Transactions on Geoscience and remote sensing, 44, 2374-2383, 2006.

Qiao, B., Zhu, L., and Yang, R.: Temporal-spatial differences in lake water storage changes and their links to climate change throughout the Tibetan Plateau, Remote Sensing of Environment, 222, 232-243, 2019.

Reinosch, E., Buckel, J., Dong, J., Gerke, M., Baade, J., and Riedel, B.: InSAR time series analysis of seasonal surface displacement dynamics on the Tibetan Plateau, The Cryosphere, 14, 1633-1650, 2020.

~~Shi, Y., Liu, C., and Wang, Z.: Concise Glacier Inventory of China Shanghai Popular Science Press, Shanghai, 89-100 pp.2005.~~

Shiklomanov, N. I., Streletskiy, D. A., Little, J. D., and Nelson, F. E.: Isotropic thaw subsidence in undisturbed permafrost landscapes, Geophysical Research Letters, 40, 6356-6361, 2013.

Song, C., Huang, B., Richards, K., Ke, L., and Hien Phan, V.: Accelerated lake expansion on the Tibetan Plateau in the 2000s: Induced by glacial melting or other processes?, Water Resources Research, 50, 3170-3186, 2014.

Streletskiy, D. A., Shiklomanov, N. I., Little, J. D., Nelson, F. E., Brown, J., Nyland, K. E., and Klene, A. E.: Thaw subsidence in undisturbed tundra landscapes, Barrow, Alaska, 1962–2015, Permafrost and Periglacial Processes, 28, 566-572, 2016.

Sun, F., Ma, R., He, B., Zhao, X., Zeng, Y., Zhang, S., and Tang, S.: Changing Patterns of Lakes on The Southern Tibetan Plateau Based on Multi-Source Satellite Data, Remote Sensing, 12, 3450, 2020.

Tong, K., Su, F., and Xu, B.: Quantifying the contribution of glacier meltwater in the expansion of the largest lake in Tibet, Journal of Geophysical Research: Atmospheres, 121, 11,158-111,173, 2016.

~~Tough, J., Blacknell, D., and Quegan, S.: A statistical description of polarimetric and interferometric synthetic aperture radar data, Proceedings of the Royal Society of London. Series A: Mathematical and Physical Sciences, 449, 567-589, 1995.~~

Treichler, D., Kääb, A., Salzmann, N., and Xu, C.-Y.: Recent glacier and lake changes in High Mountain Asia and their relation to precipitation changes, The Cryosphere, 13, 2977-3005, 2019.

Usai, S.: A least squares database approach for SAR interferometric data, Geoscience and Remote Sensing, IEEE Transactions on, 41, 753-760, 2003.

~~Wan, W., Long, D., Hong, Y., Ma, Y., Yuan, Y., Xiao, P., Duan, H., Han, Z., and Gu, X.: A lake data set for the Tibetan Plateau from the 1960s, 2005, and 2014, Scientific data, 3, 1-13, 2016.~~

Wu, Z., Zhao, L., Liu, L., Zhu, R., Gao, Z., Qiao, Y., Tian, L., Zhou, H., and Xie, M.: Surface-deformation monitoring in the permafrost regions over the Tibetan Plateau, using Sentinel-1 data, Sciences in Cold and Arid Regions, 10, 114-125, 2018.

Yang, ~~R., Zhu, L., Wang, J., Ju, J., Ma, Q., Turner, F., and Guo, Y.: Spatiotemporal variations in volume of closed lakes on the Tibetan Plateau and their climatic responses from 1976 to 2013, Climatic Change, 140, 621-633, 2017.~~

~~Yang,~~ Y., Wu, Q., Yun, H., Jin, H., and Zhang, Z.: Evaluation of the hydrological contributions of permafrost to the thermokarst lakes on the Qinghai–Tibet Plateau using stable isotopes, Global and planetary change, 140, 1-8, 2016.

Yang, Y., Wu, Q., Jin, H., Wang, Q., Huang, Y., Luo, D., Gao, S., and Jin, X.: Delineating the hydrological processes and hydraulic connectivities under permafrost degradation on Northeastern Qinghai-Tibet Plateau, China, Journal of hydrology, 569, 359-372, 2019.

Zhang, G.: The lakes larger than 1km2 in Tibetan Plateau (V2.0) (1970s-2018) [dataset], 10.11888/Hydro.tpdc.270303, 2019.

Zhang, G., Chen, W., and Xie, H.: Tibetan Plateau's lake level and volume changes from NASA's ICESat/ICESat-2 and Landsat Missions, Geophysical Research Letters, 46, 13107-13118, 2019a.

Zhang, G., Yao, T., and Kang, S.: Water balance estimates of ten greatest lakes in China using ICESat and Landsat data (in Chinese), Chin Sci Bull, 58, 2664-2678, 2013.

Zhang, G., Bolch, T., Chen, W., and Crétaux, J.-F.: Comprehensive estimation of lake volume changes on the Tibetan Plateau during 1976–2019 and basin-wide glacier contribution, Science of the Total Environment, 772, 145463, 2021a.

Zhang, G., Ran, Y., Wan, W., Luo, W., Chen, W., Xu, F., and Li, X.: 100 years of lake evolution over the Qinghai–Tibet Plateau, Earth System Science Data, 13, 3951-3966, 2021b.

Zhang, G., Yao, T., Shum, C., Yi, S., Yang, K., Xie, H., Feng, W., Bolch, T., Wang, L., and Behrangi, A.: Lake volume and groundwater storage variations in Tibetan Plateau's endorheic basin, Geophysical Research Letters, 44, 5550-5560, 2017.

Zhang, G., Yao, T., Xie, H., Yang, K., Zhu, L., Shum, C., Bolch, T., Yi, S., Allen, S., and Jiang, L.: Response of Tibetan Plateau's lakes to climate changes: trend, pattern, and mechanisms, Earth-Science Reviews, 103269, 2020.

Zhang, Y., Fattahi, H., and Amelung, F.: Small baseline InSAR time series analysis: Unwrapping error correction and noise reduction, Computers & Geosciences, 133, 104331, 2019b.

Zhang, Y., Xie, C., Wu, T., Zhao, L., Wu, J., Wu, X., Li, R., Hu, G., Liu, G., and Wang, W.: New permafrost is forming on the exposed bottom of Zonag Lake on the Qinghai-Tibet Plateau, Science of The Total Environment, 152879, 2022.

Zhao, L. and Sheng, Y.: Permafrost and environment changes on the QinghaiTibetan Plateau (in Chinese), Science Press, Beijing, China2019.

Zhao, L., Hu, G., Zou, D., Wu, X., Ma, L., Sun, Z., Yuan, L., Zhou, H., and Liu, S.: Permafrost Changes and Its Effects on Hydrological Processes on Qinghai-Tibet Plateau (in Chinese), Bulletin of the Chinese Academy of Sciences, 34, 1233-1246, 2019.

Zhao, L., Zou, D., Du, E., Hu, G., Pang, Q., Xiao, Y., Li, R., Sheng, Y., Wu, X., Sun, Z., Wang, L., Wang, C., Ma, L., Zhou, H., and Liu, S.: Changing climate and the permafrost environment on the Qinghai-Tibet (Xizang) Plateau, Permafrost and Periglacial Processes, 10.1002/ppp.2056, 2020.

Zhou, H., Zhao, L., Tian, l., Wu, Z., Xie, M., Yuan, L., Ni, J., Qiao, Y., Gao, Z., and Shi, J.: Monitoring and analysis of surface deformation in the permafrost area of Wudaoliang on the Tibetan Plateau based on Sentinel-1 data (in Chinese), Journal of Glaciology and Geocryology, 41, 525-536, 2019.

Zhu, L., Zhang, G., Yang, R., Liu, C., Yang, K., Qiao, B., and Han, B.: Lake Variations on Tibetan Plateau of Recent 40 Years and Future Changing Tendency (in Chinese), Bulletin of the Chinese Academy of Sciences, 34, 1254-1263, 2019a.

Zhu, L., Wang, J., Ju, J., Ma, N., Zhang, Y., Liu, C., Han, B., Liu, L., Wang, M., and Ma, Q.: Climatic and lake environmental changes in the Serling Co region of Tibet over a variety of timescales, Science Bulletin, 64, 422-424, ~~2019~~2019b.

Zou, D., Zhao, L., Yu, S., Chen, J., Hu, G., Wu, T., Wu, J., Xie, C., Wu, X., and Pang, Q.: A new map of permafrost distribution on the Tibetan Plateau, The Cryosphere, 11, 2527, 2017.

Zwieback, S. and Meyer, F. J.: Top-of-permafrost ground ice indicated by remotely sensed late-season subsidence, The Cryosphere, 15, 2041-2055, 2021.

Appendix

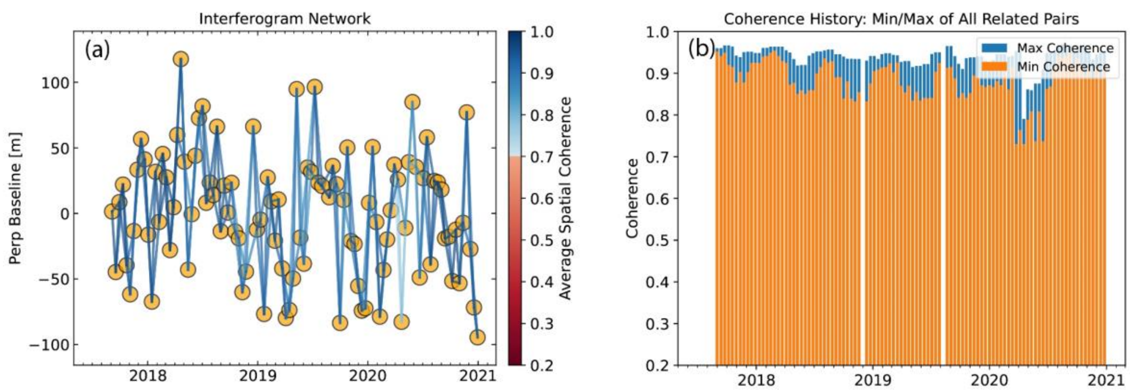

Fig. A1 (a) Network of interferograms for deformation time series estimation, color-coded by average coherence of the interferograms. Circles represent the acquisition dates, and lines represent the interferograms. (b) Average coherence of all related pairs for each SAR acquisition date.

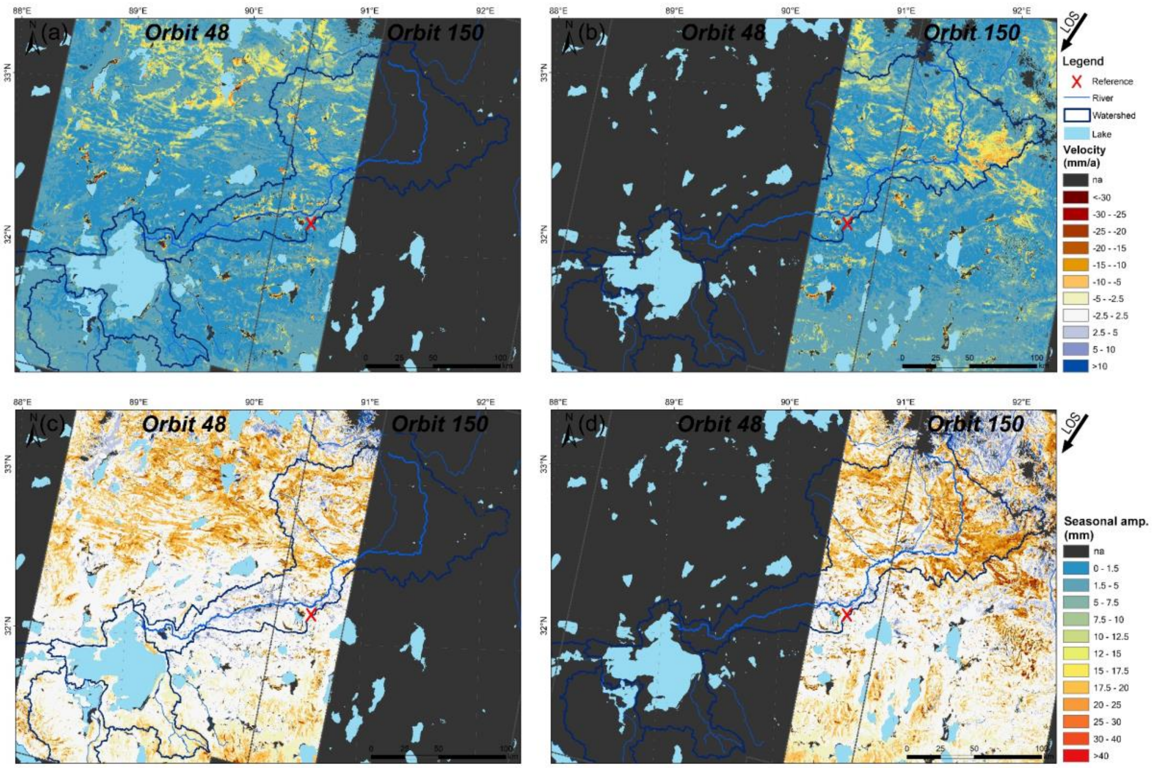

Fig. A2 Map of the periodic (seasonal) amplitude (a)(b) and long-term velocity (c)(d) retrieved from orbit 48 (a)(c) and orbit 150 (b)(d), respectively, all are in the satellite LOS direction.

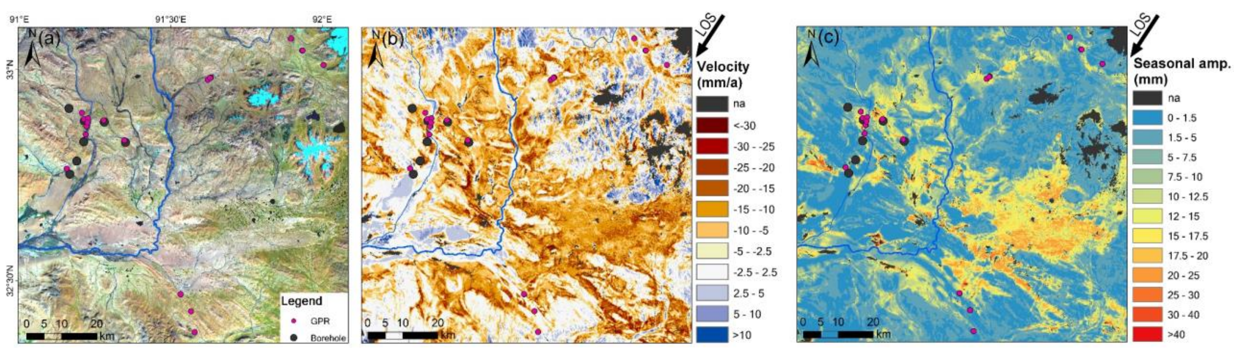

Fig. A3 Maps of the GPR and borehole regions, (a) Landsat 8 image acquired in October 2020 (red: SWIR1, green: NIR, blue: red), with GPR and borehole sites marked, (b) long-term deformation velocity, (c) seasonal deformation amplitude.

~~**Table 8 Characteristics of terrain subsidence in the Serling Co basin.**~~

~~Basin~~	~~Average (mm)~~	~~Percentage of subsidence levels (%)~~				
		~~-5 ~ -2.5 mm~~	~~-10 ~ -5 mm~~	~~-20 ~ -10 mm~~	~~-30 ~ -20 mm~~	~~< -30 mm~~
~~Zhajiazangbu subbasin~~	~~-9.1~~	~~22.4~~	~~43~~	~~30.7~~	~~3.5~~	~~0.4~~

Boquzangbu subbasin	-5.7	58.6	30.7	9.7	0.9	0.1
Overall	-9	23.4	42.6	30.2	3.4	0.4

Table 9 Potential water contribution of ground ice melting.

Basin	**Water volume (10^6 m^3/a)**				**Runoff depth (mm)**		
	subsidence signal	uplift signal	after balance[1]	after balance[2]	Water released by melting of ground ice	after balance[1]	after balance[2]
Zhajiazangbu subbasin	55.4	11.8	43.6	67.2	3.4	2.7	4.2
Boquzangbu subbasin	0.6	2.7	-2.1	3.4	0.1	-0.4	0.6
Overall	56.0	14.6	41.4	70.6	2.6	1.9	3.3
Ratio of lake volume increasement	11.3%		8.3%	14.2%			

"after balance[1]" assumes all the uplift signals were caused by permafrost ground ice aggradation, thereby subtracting from the value of the subsidence signal.

"after balance[2]" assumes all the uplift signals were caused by the rise of the groundwater table, which is recharged by melting of ground ice infiltration, thereby adding to the value of the subsidence signal.